CONSOLIDATION STUDY OF Ti-Fe ELEMENTAL POWDERS DURING HOT ISOSTATIC PRESSING BY TIME-LAPSE X-RAY COMPUTED TOMOGRAPHY

Jiaqi Xu[1], Xun Zhang[1], Vahid Nekouie[2], Michael Preuss[1,3], Philip J. Withers[1]

1: Henry Royce Institute, Department of Materials, University of Manchester, M13 9PL, UK.
2: Materials and Engineering Research Institute, Department of Engineering and Mathematics, Sheffield Hallam University, S1 1WB, UK
3: Department of Materials Science and Engineering, Monash University, Clayton, Vic-3800, Australia

Ti-Fe binary alloys have the potential of being low-cost, high-strength Ti-alloys. However, segregation of Fe during solidification complicates the melt processing of these alloys. On the other hand, the high solid-state diffusion rate of Fe in Ti makes these alloys suitable candidates for solid-state processing. One promising route for the fabrication of Ti-Fe binary alloys is Hot Isostatic Pressing (HIP) of cost-effective elemental powder mixtures. While HIP is a well-established processing technique, the detailed consolidation and diffusion processes remain unclear for mixed powders such for Ti and Fe. In this work, we focus on the consolidation of a Ti-5wt.% Fe powder mixture during HIP using time-lapse X-ray computed tomography (CT). Specifically, a miniature canister has been designed that allows sufficient X-ray penetration. In order to follow the consolidation process, the same location within the powder mixture has been CT scanned repeatedly over increasing numbers of HIP cycles where temperature and pressure have been increased incrementally. In this way particle consolidation, particle re-arrangement, rotation and compaction have been traced along with the internal porosity have been tracked as the loose powder mixture is consolidated to a fully dense solid. Densification has been observed to start at the centre while significant consolidation is observed only after the applied pressure exceeded 80 MPa with a maximum temperature of 700°C. This is believed to be a result from the shielding of the steel canister wall. These findings demonstrate how non-destructive X-ray imaging can provide valuable insights into the consolidation of powders during HIPping. This study opens the way for the production of novel difficult to cast alloys by HIPping and solid-state diffusion.

Keywords: Powder consolidation, Hot isostatic pressing, X-ray computed tomography.

1. Introduction

β-Titanium alloys are widely used for chemical, biomedical and structural applications because of their superior mechanical properties, high specific strength, good corrosion resistance, biocompatibility and chemical stability [1]. The β-Ti phase is stabilised in these alloys at room temperature by the addition of β-stabilising alloying elements such as Cr, Mo, V and Nb. However, the cost of these alloys associated with these additions is the main barrier to the wider application and development of β-Ti alloys [2]. Fe, as a cheaper and strong β-Ti stabiliser, has been considered as a potential alloying element to make high strength, low-cost β-Ti binary alloy [3]–[5]. However, severe chemical segregation during solidification makes such alloys difficult to cast.

By taking advantage of high solid-state diffusion rate of Fe in both α and β titanium phases, solid-state processing is an attractive option for making Ti-Fe alloys from low-cost blended elemental [6], [7]. In this respect, hot isostatic pressing processing (HIPping) is a well-established and cost-efficient technique for producing near-net shape components out of materials that are difficult to cast [8]. As a solid-state processing routine, HIPping can be used to manufacture hard-to-cast alloys below their melting point and avoid chemical segregation [9]. Further, HIPping can be used to make non-equilibrium microstructures [10], [11] or to manufacture composites [12]–[14].

During HIPping, temperature and pressure are applied simultaneously to the powder mixture. The applied pressure leads to localised plastic flow which is further boosted by the lowering of the yield strength as the temperature rises [15]. As a thermally activated process, diffusion kicks in during the later stages of HIPping at relatively high temperatures. In this regime densification is dominated by diffusion-assisted material transport [9]. The aim of this paper is to focus on the early stage of the HIPping i.e. powder densification process during consolidation to examine its potential for the production of Ti-Fe alloys.

In the context of optimising the HIPping process, X-ray computed tomography (CT) enables the tracking of the full geometry and the internal microstructure change to be compared prior to, and after, consolidation [15]–[18]. Adam et al. [18] have compared the residual porosity determined by X-ray CT from scanning extracted thin rods from HIPped products for 316 stainless steel (SS) being HIPped at various temperatures. Tammas-Williams et al. applied X-ray CT to track pore closure in additively manufactured Ti-6Al-4V components after a HIPping cycle [15]. Time-lapse X-ray CT can record detailed information on the microstructural evolution and the overall morphology change before, during and after HIPping providing insight into the role of the material properties, initial microstructure and the HIPping conditions on the HIPping response e.g. on the evolution of compaction and morphology.

Here we focus on the consolidation of a Ti-5wt.% Fe powder mixture during HIPping using time-lapse interrupted X-ray CT. A miniature HIP canister has been designed to allow sufficient X-ray penetration for metal powders together with high spatial resolution. Once filled, the miniature canister has been X-ray CT scanned repeatedly in between HIPping cycles employing successively increasing temperature and pressure steps. By comparing the X-ray CT virtual slices/volumes taken at different stages of early stage of HIPping, the individual particle rotation, movement and compaction have been traced along with the internal porosity/density change till the loose powder mixture is fully consolidated.

2. Experimental Methods

2.1. Materials and HIPping

The loose powder mixture consisted of commercially pure (CP) titanium powder mixed with 5 wt.% of iron powder. The CP titanium (Grade 1) powder provided by Carpenter Additive has a diameter distribution from 15 µm to 45 µm. The 99.0% Iron powder was provided by Goodfellow with a diameter range below 60 µm. The Ti+5 wt.% Fe powder mixture was blended by 4-hour vibration in a custom-made vibration mill. In order to undertake time-lapse X-ray CT, the Ti+5 wt.% Fe powder mixture was placed in a specially designed miniature HIP canister (shown in Figure 1) made from SS316 stainless steel with an inner diameter of 2 mm, wall thickness of 0.5 mm and 30 mm length. Medium mild steel canisters (25 mm in diameter, 2 mm in wall thickness and 30 mm in length) were also HIPped together with the miniature canister for post-mortem characterisation. The canisters were filled with powder mixture under argon protective environment and degassed at ambient temperature followed by hot crimping the evacuation tube (see Figure 1).
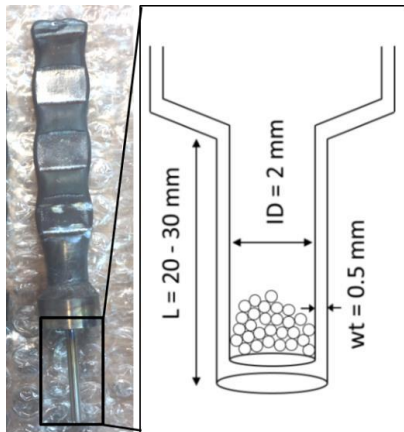

Figure 1. Photograph and schematic showing the miniature can for high-resolution time-lapse X-ray CT of powder densification during HIPping.

HIPping was conducted using an AIP8-45H Hot Isostatic press in the Royce Translational Centre, at the University of Sheffield. Prior to the time-lapse experiment, a benchmark HIPping cycle at 800°C and a peak pressure of 100 MPa without any dwell time was conducted on a medium mild steel canister. The Ti-Fe powder compact reached full density after this HIPping cycle which implied that these parameters could be used as the end point of the HIP cycles in the time-lapse densification study. As summarised in Table 1, progressively severe HIPping steps were performed starting at 400°C and 20 MPa and rising to 800°C and 100 MPa. A heating rate of 5°C/min was applied throughout with no dwell time upon reaching the target temperature and pressure followed by immediate cooling at -15°C/min for all HIPping cycle.

Table 1: The record of the conditions used in HIPping cycles.

HIPping Cycle No.	Temperature/°C	Pressure/MPa
1	400	20
2	450	30
3	500	40
4	550	50
5	575	55
6	600	60
7	625	65
8	650	70
9	675	75
10	700	80
11	750	90
12	800	100

2.2. X-ray Computed Tomography

X-ray CT scans were performed on the filled canister before HIPping and after each HIPping step, focusing on the same location within the canister to track the change in between HIPping cycles. The X-ray CT scans were performed using a Zeiss VersaXRM520 scanner in the Henry Moseley X-ray Imaging Facility, part of the National Research Facility in X-ray CT at the University of Manchester. The X-ray source was operated at an accelerating voltage of 140 kV and a power of 10W. For each scan, 3601 projections were collected as the sample was rotated incrementally over 360°. The optics and source-to-sample and sample-to-detector distances were adjusted to give 4 times magnification resulting in a voxel size of 1.14 x 1.14 x 1.14 µm^3 in the reconstructed volume and a field of view of 2.3 x 2.3 x 2.3 µm^3.

2.3. Scanning Electron Microscopy

The HIPped medium mild steel canister (25 mm in diameter, 2 mm in wall thickness and 30 mm in length) was sliced using a Struers Accutom-5 cut-off machine. Cross-section of the canister was prepared for scanning electron microscope (SEM) investigation. Samples were

ground using SiC paper incrementally from grit 600 to 4000 followed by polishing using a mixture of colloidal silica suspension (OPS) with hydrogen peroxide at a volume ratio of 4:1 till the sample surface was scratch-free under an optical microscope. BSE image and EBSD mapping of the polished sample surfaces were collected under an accelerating voltage of 20 kV on FEI Magellan and Tescan Mira3 equipped with the symmetry detector and Aztec EBSD system from Oxford Instrument.

3. Results and Discussion

3.1. *Powder particle rearrangement*

X-ray CT virtual slices through the centre of the miniature canister are shown in Figure 2. Comparing the particle arrangement before HIPping and after 2 cycles it is evident that the densification of the powders is very limited at this stage due to the relatively low temperature and pressure that has been applied. Some particle rearrangement can be observed where the initial powder packing density was relatively low, as indicated by the arrow and ellipse in Figure 2.
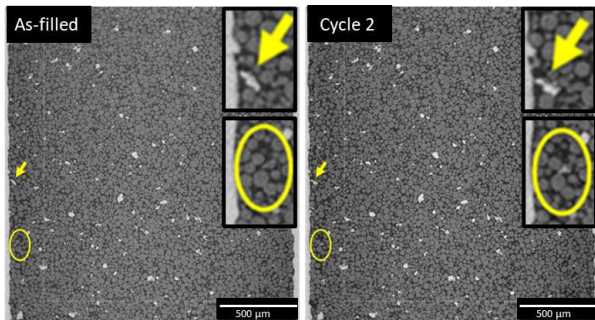
Figure 2. Identical X-ray CT virtual slices taken along the length direction through the centre of the miniature canister: As filled (left) and after two HIP cycles (right). The grey levels represent; mid-grey – titanium, light grey – iron, dark grey – air/porosity with the light grey canister wall just within the field of view. The arrow and ellipse highlight localised particle rearrangement.

3.2. *Powder Densification*

Figure 3 shows the progress of compaction inside the miniature canister after 7 (625°C 65 MPa), 8 (650°C 70 MPa), 9 (675°C 75 MPa) and 10 (700°C 80 MPa) HIPping cycles. After 8 HIPping cycles, deformation of the canister started to be observed clearly as the internal wall is no longer perfect cylindrical. After 10 HIPping cycles, significant deformation is observed. It is also noteworthy that the powder mixture is still relatively loose, but the canister has started showing visible non-isotropic deformation under compaction.
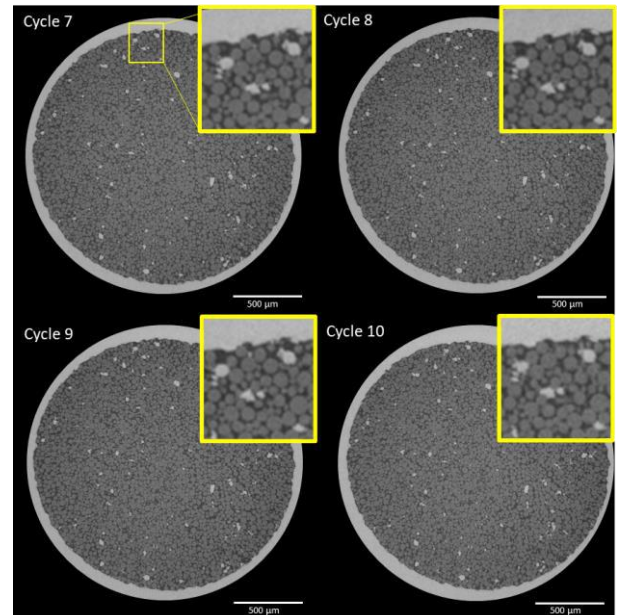

Figure 3. Region of interest X-ray CT cross-sectional virtual slice through the centre of the miniature canister: after 7 (625°C 65 MPa), 8 (650°C 70 MPa), 9 (675°C 75 MPa) and 10 (700°C 80 MPa) cycles. The grey levels represent; mid-grey – titanium, light grey – iron, dark grey – air/porosity with the canister also light grey.

The packing density for the central part of the canister and at the periphery, close to the canister wall, have been quantified separately from the X-ray CT datasets and plotted in Figure 4 for all the HIPping cycles. It is evident that the particle movement is larger at the periphery from virtual slices while the density change occurs first in the centre (see Figure 4). Care needs to be taken when assessing the density because of segmentation issues and beam hardening, but the results show that, to within experimental error, the densities at the centre and periphery are similar over the early stages and largely unchanged from the initial values. Significant densification is not observed until the 10th cycle where the applied pressure exceeded 80 MPa with a maximum temperature of 700°C is believed to be a result from the shielding by the stainless steel 316 canister wall which has higher temperature strength than mild steel [19]. Nevertheless, one can see that the centre densifies somewhat ahead of the periphery and that full density is reached by cycle 12 (800°C and 100 MPa). In addition, iron particle has been found not yet diffused much till this full-dense stage which indicates that densification happens first while the diffusion of iron follows later during HIPping.
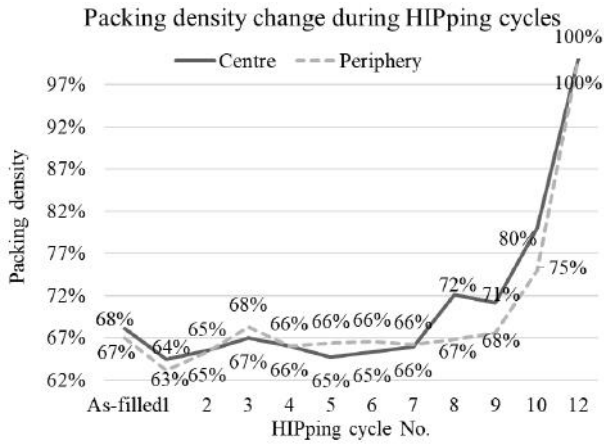
Figure 4. The packing density at the centre and the periphery determined from the X-ray CT scans over the successive HIPping cycles.

3.3. *Canister morphology changes*

The change in the shape of the miniature canister before and after the HIPping cycles is evident from the X-ray CT slices in Figure 6 which shows very uneven contraction of the can. Indeed, the deformation of the can along one diagonal is significantly larger than for the perpendicular diagonal. The primary reason for this is that as-manufactured the internal and external diameters of the can were not concentric thereby offering variable resistance to the HIP pressure in different directions resulting in uneven deformation during HIPping.
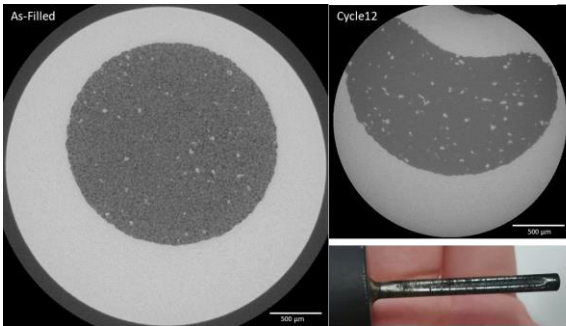
Figure 6. Left: The global X-ray CT scan of the as-filled miniature canister. The grey levels represent; mid-grey – titanium, light grey – iron, dark grey – air/porosity showing the non-concentric internal and external cannister walls (light grey). Right: HIPped miniature canister after 12 HIPping cycles (800°C 100 MPa).

3.4. *Final compacted microstructure*

Figure 5 shows the final compacted microstructure (HIPped under 800°C and 100 MPa). It's clear that the originally spherical titanium powders have been completely consolidated as a matrix while the irregular-shaped iron particles (light grey) have maintained their shape and sit in between the alpha titanium (dark grey) matrix. A shell of beta titanium (mid-grey) surrounding iron particles has been found stabilised at room temperature as a result of limited iron diffusion. This indicates that the loose Ti-Fe powder mixture

consolidated first while the diffusion only starts at the highest temperatures allowing the iron to redistribute.
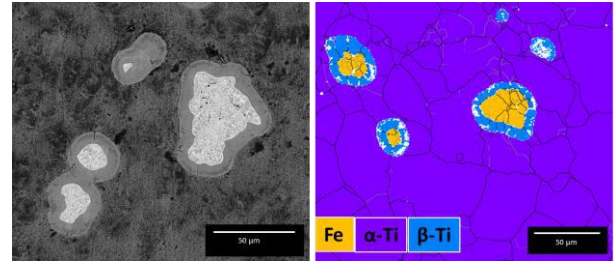

Figure 5. The BSE image (left) and phase map (right) of final compacted microstructure after HIPping at 800°C 100 MPa. The grey levels (left) represent; dark grey – alpha titanium, mid-grey – beta titanium, light grey – iron.

4. Conclusions

Consolidation of a Ti-5wt.% Fe powder mixture during HIPping has been successfully tracked using time-lapse X-ray CT. By comparing the X-ray CT datasets taken at different stages of consolidation, particle re-arrangement, densification and morphology evolution have been captured and quantified along with the internal porosity change from loose powder to fully consolidated solid. This work brings the potential for the production of novel difficult to cast alloys by HIPping and solid-state diffusion.

Under relatively low applied pressure and temperature (< 625°C and 65 MPa), only particle re-arrangement has been observed with no significant compaction or change in morphology of the loose powder mixture. Densification has been found to start at the centre upon reaching 650°C and 70 MPa. Significant densification has been observed once the applied pressure exceeded 80 MPa with a maximum temperature of 700 °C. This is believed to be delayed somewhat compared to that for a mild steel can as a result of the shielding of the steel canister wall. This experiment validates the power of non-destructive X-ray imaging as a promising technique to provide valuable insights into the consolidation of mixed powders during HIPping.

5. Acknowledgements

6. References

1. C. Leyens and M. Peters, *Titanium and Titanium Alloys*, 1st ed. John Wiley & Sons, Ltd, 2003.
2. 'Low-cost titanium alloys? Iron may hold the answers - ScienceDirect'. https://www.sciencedirect.com/science/article/pii/S0026065709700402 (accessed Feb. 23, 2023).
3. G. Lütjering and J. C. Williams, *Titanium*. in Engineering Materials, Processes. Berlin, Heidelberg: Springer, 2007.
4. L. Bolzoni, E. M. Ruiz-Navas, and E. Gordo, *Materials & Design*, vol. 110, pp. 317–323, Nov. 2016.
5. D. V. Louzguine, H. Kato, L. V. Louzguina, and A. Inoue, *Journal of Materials Research*, vol. 19, no. 12, pp. 3600–3606, Dec. 2004.
6. D. V. Louzguine-Luzgin, L. V. Louzguina-Luzgina, H. Kato, and A. Inoue, *Acta Materialia*, vol. 53, no. 7, pp. 2009–2017, Apr. 2005.
7. J. O'Flynn and S. F. Corbin, *Journal of Alloys and Compounds*, vol. 618, pp. 437–448, Jan. 2015.
8. C. Boberski, 'Hot Isostatic Processing, By H. V. Atkinson and B. A. Rickinson, Adam Hilger, Bristol 1991, 190 pp, ISBN 0-7503-0073-6', *Advanced Materials*, vol. 4, no. 4, pp.312–313, 1992.
9. H. V. Atkinson and S. Davies, *Metall Mater Trans A*, vol. 31, no. 12, pp. 2981–3000, Dec. 2000.
10. M. S. El-Eskandarany, S. Ishihara, W. Zhang, and A. Inoue, *Metall Mater Trans A*, vol. 36, no. 1, pp. 141–147, Jan. 2005.
11. A. Huang, D. Hu, M. H. Loretto, J. Mei, and X. Wu, *Scripta Materialia*, vol. 56, no. 4, pp. 253–256, Feb. 2007.
12. C. Cai *et al.*, *Composites Part B: Engineering*, vol. 164, pp. 546–558, May 2019.
13. S. C. Tjong and K. C. Lau, *Composites Science and Technology*, vol. 59, no. 13, pp. 2005–2013, Oct. 1999.
14. D. Roy, R. Mitra, O. A. Ojo, W. Lojkowski, and I. Manna, *Metall Mater Trans A*, vol. 42, no. 8, pp. 2498–2508, Aug. 2011.
15. S. Tammas-Williams, P. J. Withers, I. Todd, and P. B. Prangnell, *Metall Mater Trans A*, vol. 47, no. 5, pp. 1939–1946, May 2016.
16. S. A. McDonald *et al.*, *Materials Characterization*, vol. 172, p. 110814, Feb. 2021.
17. S. Tammas-Williams, P. J. Withers, I. Todd, and P. B. Prangnell, *Scripta Materialia*, vol. 122, pp. 72–76, Sep. 2016.
18. A. J. Cooper, O. C. G. Tuck, S. A. J. Armson, and M. Preuss, in *Volume 6A: Materials and Fabrication*, San Antonio, Texas, USA: American Society of Mechanical Engineers, Jul. 2019, p. V06AT06A001.
19. R. M. McMeeking, *Int. Journal of Mechanical Sciences*, vol. 34, no. 1, pp. 53–62, Jan. 1992.

QUASI IN-SUIT STUDY OF MICROSTRUCTURE EVOLUTION AND MECHANICAL PROPERTIES IN TI6AL4V ALLOY METAL INJECTION MOLDING

Wanli Ren[1], Xiaolong Chen[1,2], Hui Chang[1,2*], Zhengfei Zhou[1,2*]

1 The college of Material Science and Engineering, Nanjing Tech University ,Nanjing, China.
2 Shangi institute for advanced materials (nanjing) Co.,LTD, Nanjing, China.

Metal injection molding (MIM) as the fifth generation of manufacturing process, with higher material utilization rate and more efficiency of forming complex components, has been used in the electronics, transportation industry et al. widely. MIM titanium alloys are more used in appearance, none stress parts. The poor mechanical properties restrict the development of MIM, especially plastic properties. In this paper, the evolution of the microstructure of MIM-Ti6Al4V alloy powder by adjusting sintering temperature, time and pressure was investigated by a quasi-in-situ method with vacuum encapsulation technique, and the relationship between sintering parameters-microstructure-mechanical properties was also verified. Conclusions are as follows: Porosity decreases with increasing temperature and time, the transition time from the connected state to the closed and spherical state of the pores shortens with increasing temperature, and the sintering densification effect in the low-pressure state is better than that in the high-pressure sintering. At the same time, with the increase of temperature and time, the slate-like α-phase rapidly dissolves back into the β-phase, and then transforms into the needle-like α-phase, and the proportion of α-phase also decreases, and the grain size of β-phase grows significantly, but the speed of dissolves is slower at low temperature; the tensile strength and elongation of Ti6Al4V alloy are stable at 950MPa and 12%, respectively, using the sintering parameters of 1200°C, 10^{-1}pa, and 4h. The study of this work is conducive to MIM titanium alloy play a more important role in stress parts and promote the process of advanced lightweight equipments.

Keywords: MIM, Quasi in-suit, Microstructure, Sintering parameter, Ti6Al4V, Mechanical property

1. Introduction

Titanium alloy is widely used as a key component material for transportation, aerospace, deep-sea space, weaponry and other fields of equipment because of its high specific strength, good corrosion resistance and many other advantages[1], but due to poor thermal conductivity, low modulus of elasticity, strong chemical activity and other characteristics, there are problems such as high processing difficulty, low material utilization and long production cycle when process complex titanium alloy parts using traditional processes[2]. The development of metal powder injection moulding (MIM) technology has provided a new solution to the problems in the processing of titanium alloys, especially small batch sizes and complex structural titanium alloy components. However, in the global MIM market of tens billions dollar, titanium alloy products have only a small share, and the MIM market in China only accounts for 0.4%[3].

Titanium alloy in the MIM market, in addition to the cost constraints, but also by the feedstock preparation, injection molding, debinding, sintering and other processes, experts and scholars have carried out a lot of relevant research[4-7], but the porosity of the sintered sample, microstructure, impurity element content, etc. are the final impact factors of the MIM titanium alloy service performance. These factors are inseparable from the characteristics of the powder and the sintering process. Therefore, lots of researchers have tried to use fine powder (0-45μm) sintering, adding TiH2, HDH-Ti powder, adjusting the sintering process parameters, using hot isostatic pressing (HIP), shot blasting and other

techniques, which have made a lot of contributions to reduce the porosity of MIM sintered samples, improve the microstructure and reduce the content of impurity elements, and also make the service performance of MIM titanium alloy to be greatly improved, but at present most of the commercial MIM titanium alloys are still only used as non-load bearing parts.

Kusaka[8] and Hu[9] evaluated the sintering behaviour of MIM gas atomic (GA)-Ti powders and mechanically crushed Ti powders and found that the finer the powder size, the lower the porosity of the sintered sample and the higher the tensile strength. Miura[10], Ibrahim[6] and Ferri[11,12] all chose Ti-6Al-4V pre-alloyed GA powders with particle size less than 45 μm. The studies were carried out and all were able to obtain sintered bodies with porosity <5%, tensile strength >800 MPa and elongation >5%.

Although researchers have carried out amount of work on the sintering of MIM titanium alloys, most of them only focused on the study of the final state of MIM sintering, without really revealing the evolution law of microstructure during the sintering process. In this paper, we adopt a quasi-in-situ experimental method to clarify the microstructure evolution of MIM-Ti6Al4V during the sintering process by simulating real sintering conditions, and combine with macroscopic mechanical property testing to determine the microstructure with optimal mechanical properties and further determine the sintering process parameters. The successful development of this work not only realize the precise regulation of MIM sintering process and save a lot of experimental cost, but

also provides a theoretical basis for the engineering application of MIM-Titanium alloy.

2. Experimental process

2.1 Preparation of pre-sintered specimens

In this paper, 0-25μm GA-Ti6Al4V pre-alloyed powder is used for the preparation of MIM feedstock, and the powder composition and characteristic particle sizes are shown in Table 1.

Table 1 Composition and characteristic particle sizes of 0-25 μm GA-Ti6Al4V pre-alloyed powders

Chemical composition(wt.%)							Particle size(μm)		
Ti	Al	V	O	N	H	Fe	D_{10}	D_{50}	D_{90}
Bla.	6.0	4.0	0.1	0.0	0.0	0.0	8.9	14.3	22.0

According to the vibration density of the powder 2.77g/cm^3, the ratio of powder to binder (mass ratio) was determined to be 84:16, where the binder was mainly polyformaldehyde, supplemented by polypropylene (PP), high density polyethylene (HDPE), ethylene acrylic acid copolymer (EAA), ethylene bis-stearamide (EBS), stearic acid (SA), paraffin wax (WAX) and benzotriazole (BTA). The preparation of the feedstock was made using the CF-3L.QFMLJ and CF-45.ZLJ type compactors and granulators respectively. The BL110FE/M225 injection molding machine was used to prepare the "dog bone" green specimens in accordance with GB/T 7963-2015 for sintered metal materials, and the STZ-400L-0A catalytic debinding machine was used to prepare the brown specimens, in which oxalic acid was used as the catalyst, and Model VM30/30/60-M metal vacuum sintering furnace was used to carry out negative pressure thermal debingding, holding at 900°C for 0.5h, and finally the pre-sintered specimens with certain porosity (73.3%, relative to the theoretical density) and strength were obtained, the fracture of the pre-sintered specimen as shown in Fig. 1.
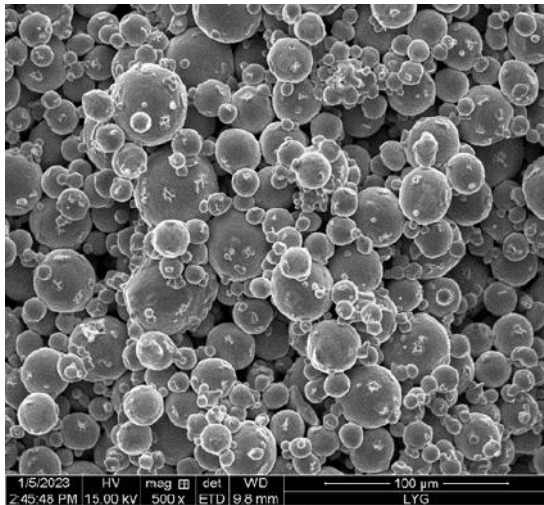

Fig. 1 SEM image of the fracture of the pre-sintered specimen

2.2 Quasi in-situ sintering sample preparation

Subsequently, the pre-sintered specimens were cut into Φ4.9×5 mm specimens by EDM, and then cleaned with ethanol and dried, encapsulated into quartz tubes, which were washed three times with high purity argon gas. The sintering temperature was set to 1100, 1150 and 1200°C, the sintering time was set to 0.5, 1, 2, 3 and 4 h, the sintering pressure was set to 10^{-1}pa,30kpa, 50kpa.The quenching was then carried out with water cooling in order to obtain the microstructure in the sintered densified state.

2.3 Characterisation

The particle size distribution of the powder was characterised using Sync laser particle size meter, the elemental content of the powder was characterised using LECO ONH836 and ICP-OES, the decomposition temperature of the binder in the feedstock was characterised using STA449-F3 differential thermal analysis for the development of thermal debinding and pre-sintering curves, the densities of the pre-sintered and sintered samples were characterised using Archimedes method, and the fracture of pre-sintering specimen was characterised using a Qutanta 450 FEG SEM, CX40M metallurgical microscope was used to characterise the microstructure of the sintered samples, Rigaku 9kW XRD diffractometer was used to characterise the phase composition of the sintered samples and MTS was used to characterise the mechanical properties of the "dog bone" parts.

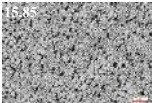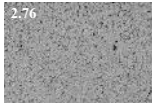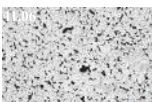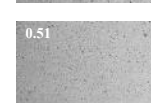## 3. Results and discussion

3.1 Pore state
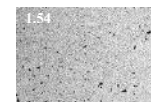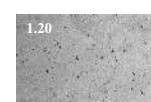
3.1.1 Effect of temperature on the pore state

It can be seen from Tables 2-4 that at the same sintering time, as the temperature rises from 1100°C to 1200°C, the porosity decreases, the densification becomes more effective and the shape of the pores develops from a connected state to a closed state as well as a spherical state, but one of the samples in Table 2 has an abnormal porosity at 1150°C sintered for 3 h. The possible reason for this is that the initial porosity of the sample at this location is higher, resulting in a higher porosity relative to 1100°C and 1200°C sintered for 3 hours. When comparing the different temperatures, it was found that the pores were basically in the form of connected pores at 1100°C, connected pores and closed pores at 1150°C, and all closed pores and spherical pores at 1200°C, and the porosity was below 5%, proving that 1200°C gives a better density compared to the other two temperatures.

3.1.2 Effect of time on the pore state

At the same temperature, as the sintering time increased from 0.5h to 4h, there was a tendency for the porosity to decrease, indicating that the longer the sintering time was, the better the densification of the sintered samples. This proves that increasing the temperature can accelerate the closure and disappearance of the pores.

Table 2 Microstructure at a sintering pressure of 10^{-1} pa

T(°C) t(h)	1100	1150	1200
0.5	15.85	2.76	1.49
1	17.01	7.08	1.54
2	11.02	0.72	1.20
3	4.91	15.66	0.51
4	4.34	1.59	0.93

3.1.3 Effect of pressure on pore state

In comparison with Table 2-4, the porosity of samples sintered at 10^{-1} pa was significantly lower than that of 30kpa and 50kpa under 1100°C-1150 sintering conditions, and the transition time from connected pores to closed pores and spherical pores was shorter than that of 30kpa and 50kpa. At a sintering temperature of 1100°C, the porosity of samples sintered at 30kpa and 50kpa was higher than 10%. The porosity decreases less significantly with increasing sintering time, whereas the porosity of the 10^{-1} pa sintered sample decreases more significantly with increasing time, although the porosity also exceeds 10% within a sintering time of 0.5 to 2 hours. As the temperature increases, especially when sintering at 1200°C, the negative effects of higher sintering pressures on densification are not as severe as at low pressures, and even some porosities are lower than low-pressure sintering.

The pore state in the sintering microstructure of 0-25 µm GA-Ti6Al4V pre-alloy powders was studied from the sintering conditions (temperature, time, pressure) and it was found that as the temperature and time increased, the porosity of the Ti6Al4V alloys decreased; as the temperature increased, the transition time from the connected to the closed and spherical state of the pores became shorter; the porosity in low-pressure sintering was lower than in higher-pressure sintering. The porosity is lower in low pressure sintering than in higher pressure sintering, but as the temperature increases, the effect of low pressure sintering densification compared to high pressure sintering is no longer significant.

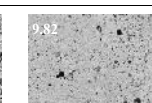**Table 3 Microstructure at a sintering pressure of 30kpa**
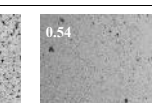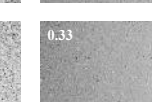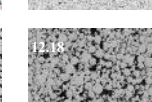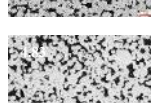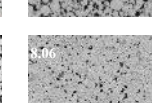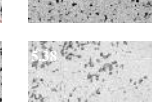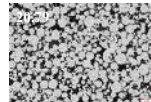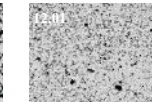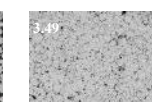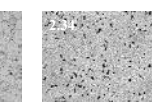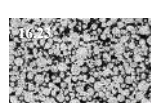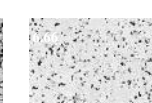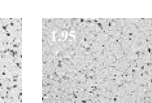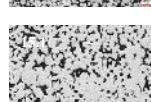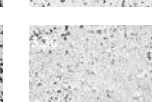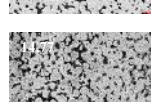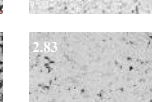
T(°C) t(h)	1100	1150	1200
0.5	17.49	9.82	0.54
1	17.22	1.33	0.33
2	13.33	12.18	0.67
3	12.37	8.06	2.37
4	14.52	2.31	1.44

Table 4 Microstructure at a sintering pressure of 50kpa

T(°C) t(h)	1100	1150	1200
0.5	20.22	12.01	3.42
1	20.22	3.49	2.54
2	16.23	1.96	1.95
3		2.36	0.25
4	14.57	2.83	0.18

3.2 Phase evolution

3.2.1 Effect of temperature on phase evolution

It was found that at 1100°C, slate-like α-phase and equiaxed β-phase were present in the microstructure, and as the temperature increased, the slate-like α-phase gradually disappeared and evolved into coarse β-phase grains as well as needle-like α'-phase by 1200°C at Tables 2-4. Moreover, the proportion of α-phase decreased with increasing sintering temperature. XRD patterns at three sintering temperatures at 10^{-1}pa and 2h are given in Figure 2. It is also evident from the XRD plots that the number of peaks representing the α-phase as well as the intensity of the peaks representing the β-phase gradually decrease and decrease as the temperature increases, while the intensity of the peaks representing the β-phase gradually increases, indicating that the α-phase is changing to the β-phase. At the same time, the grain size of the β-phase increases as the temperature increases.
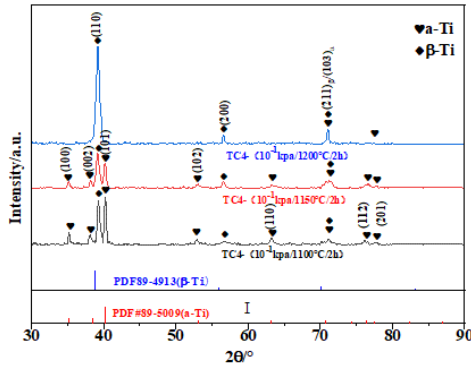
Fig.2 XRD diagram of Ti6Al4V pre-alloyed powder at different sintering temperatures and at the same sintering pressure and time

3.2.2 Effect of time on phase evolution

With the increase of sintering time, the original ungrown needle-like or slate-like α-phase in the microstructure gradually grows and has a tendency to form an equiaxial shape, and this tendency is more obvious at 1100°C. Moreover, with the increase of time, the original initial α-phase in the powder gradually dissolves back into the β-phase, resulting in the microstructure of the sintered sample being β-phase at the end of sintering, followed by quenching, which makes the needle-like α'-phase to precipitate out from the β-phase. Figure 3 shows XRD plots at 10^{-1}pa and 1200°C after different sintering times, from which both α and β-phases are present in the microstructure at 0.5h, and the α-phase basically disappears when the sintering temperature continues to 2h, at which point the whole sintered sample is supersaturation, with the increase in sintering time, the α-phase precipitates again, but at a very low proportion, as can be verified from Tables 2-4.
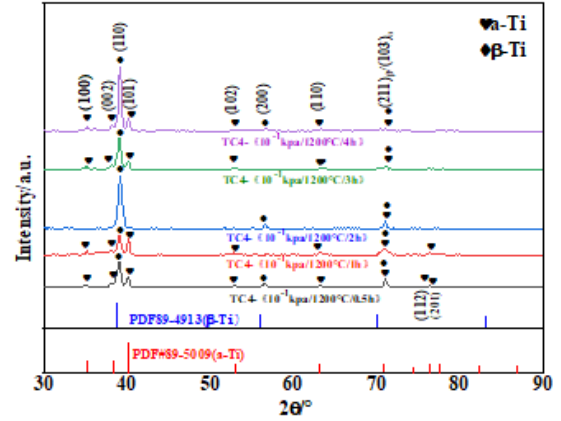
Fig.3 XRD diagram of Ti6Al4V pre-alloyed powder at different sintering times and at the same sintering temperature and pressure

3.2.3 Effect of pressure on phase evolution

It was found that at 1100°C, the slate-like α-phase evolves into the needle-like α'-phase as the pressure increases, indicating that the pressure favours the re-solution of the α-phase, thus driving down the proportion of α-phase at Tables 2-4. When the sintering temperature is increased, the α-phase in the powder will rapidly back-dissolve into the β-phase, making the change in pressure have little effect on the evolution of the phase ratio and morphology. However, it is found in Figure 4 that as the sintering pressure increases from 10^{-1}pa to 30kpa, the proportion of the α-phase becomes smaller, probably because the pressure inhibits the precipitation of the α-phase.
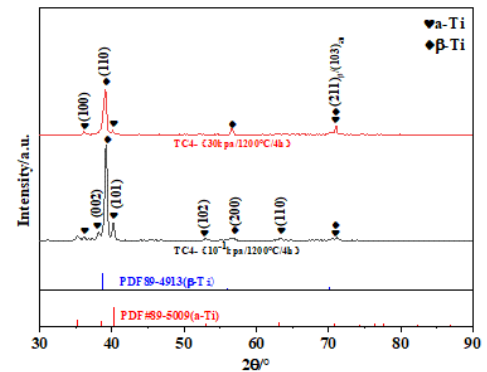
Fig.4 XRD diagram of Ti6Al4V pre-alloyed powder at different sintering pressures and at the same sintering temperature and time

It can be seen from the above that as the temperature increases, the slate-like α-phase rapidly dissolves back into the β-phase, and then changes to the needle-like α' phase, and the proportion of α-phase also decreases, while the β-phase grains appear to grow significantly; increasing the sintering time also has the same pattern, but at low temperatures, the rate of dissolution is slower; the

sintering pressure promotes the α-phase dissolution at low temperatures, but inhibits the α-phase dissolution at high temperatures. The sintering pressure promotes the re-solution of the α-phase at low temperatures, but inhibits the precipitation of the α'-phase at high temperatures.

3.3 Mechanical properties

According to the above analysis of the pore characteristics, phase ratio and morphology, the sintering parameters of 1200°C, 4 h and 10^{-1}pa were selected for the preparation of the highly densified "dog bone" parts and the mechanical properties were verified. The stress-strain curve was shown in Fig. 5, from which the tensile strengths were stable at 950 MPa and the elongation exceeded 12% after three equal tensions, indicating that the process was able to produce a titanium alloy material with excellent mechanical properties.
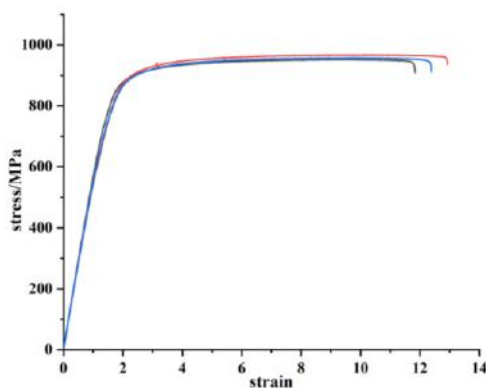
Fig.5 Stress-strain curves of standard parts prepared by the sintering process at 1200°C, 10^{-1}pa, 4h

4. Conclusion

This paper have taken use of a quasi in-situ experimental method to systematically study the microstructure evolution of GA-Ti6Al4V pre-alloy powder sintering behavior during the MIM forming process, and tensile experiments was verified that the mechanical properties of the sintered samples can be controlled by adjusting the microstructure, and the paper conducted the following conclusions:

1. The porosity of Ti6Al4V alloy decreases as the sintering temperature and time increase; as the temperature increases, the transition time of pore from connected state to closed and spherical state becomes shorter; the porosity of low-pressure sintering is lower than that of higher-pressure sintering, but as the temperature increases, the effect of low-pressure sintering densification compared to high-pressure sintering is no longer obvious;

2. As the sintering temperature increases, the slatted α-phase rapidly dissolves back into the β-phase, followed by a shift to the needle-like α-phase, and the proportion of α-phase decreases, while the β-phase grains grow significantly; the same pattern is observed when the sintering time is increased, but the rate of dissolution is slower at low temperatures; the sintering pressure promotes the dissolution of α-phase at low temperatures, but inhibits the precipitation of α-phase at high temperatures. The sintering pressure promotes the re-solution of the α-phase at low temperatures, but inhibits the precipitation of the α'-phase at high temperatures.

3. Titanium alloy materials with good comprehensive mechanical properties can be prepared by selecting sintering parameters which can form a specific microstructure.

5. Acknowledgements

6. References

1. Qiu G , Guo Y., *International Journal of Minerals, Metallurgy and Materials*, 29(2022) 599-610.
2. Cabezas-Villa J L, Lemus-Ruiz J, Bouvard D, et al., *International Journal of Minerals Metallurgy and Materials,* 25(2018) 13.
3. *https://zhuanlan.zhihu.com/p/471209295*.
4. Thavanayagam G, Swan, et al., *Powder Technology: An International Journal on the Science and Technology of Wet and Dry Particulate Systems,* (2018).
5. Nakamura H, Shimura T, Nakabayashi K, *Journal of the Japan Society of Powder and Powder Metallurgy,* 46(1999) 870-876.
6. Ibrahim R, Azmirruddin M, Jabir M, et al., *American Journal of Applied Sciences,* 7(2010):811-814.
7. Guo S, Qu X, He X, et al*., Trans Tech Publications,* (2006) 2639-2644.
8. Kusaka K, Kohno T, Kondo T, et al., *Journal of the Japan Society of Powder and Powder Metallurgy*, 42(1995) 383-387.
9. Hu K, Zou L, Shi Q, et al., *Powder Technology*, 367 (2020) 225-232.
10. Hideshi M, Teruie T, Yuki K, et al., *Journal of the Japan Society of Powder and Powder Metallurgy,* 53(2006) 815-820.
11. Ferri O M, Ebel T, Bormann R., *Materials Science & Engineering A*, 504(2009) 107-113.
12. Obasi G C, Ferri O M, Ebel T, et al., *Materials Science & Engineering A*, 527(2010) 3929-3935.

OPTIMISING TITANIUM POROUS STRUCTURES FOR HYDROGEN ELECTROLYSIS AND BEYOND

Iain Berment-Parr[1], Amanda Cruchley[1], Simon Graham[2]

1 The Manufacturing Technology Centre Ltd., Ansty Park, Coventry, CV7 9JU, UK
2 Department of Material Science and Engineering, The University of Sheffield, Mappin Street, Sheffield, S1 3JD, UK

Two innovative net-shape and additive manufacturing methods have been investigated in an attempt to optimise the fabrication of titanium porous structures. Porous Transport Layers (PTLs) are vital components in Proton Exchange Membrane (PEM) electrolysers, which are some of the most promising systems for low-cost production of green hydrogen fuel generated with zero carbon emissions. Due to the high voltage and low pH operating conditions experienced at the anode, titanium is often considered the only commercially viable material for bipolar plates and PTLs, which are sandwiched into many layers to form an electrolyser stack. As a result, titanium makes up a significant proportion of the total capital cost for the overall system, and these costs are a major economic barrier to increased hydrogen production capacity.

Previous work published by the authors has shown that the embodied carbon emissions of titanium bipolar plates and PTLs could be greatly reduced by utilising unconventional net-shape processing of titanium sponge fines or recycled powder sources. The work presented here goes further, and outlines steps taken to optimise the performance, production rate, and sustainability of titanium PTLs through a wider range of possible manufacturing routes. Each method has been used to create a demonstration bipolar plate with an integrated porous transport layer. The increased design freedom showcased by these methods has the potential to optimise fluid flow and greatly enhance the efficiency of hydrogen generation. If combined with high throughput automation of fabrication and assembly steps, they become viable options for reducing the manufacturing cost of electrolyser systems.

Beyond the hydrogen value chain, the technologies assessed could be applied to optimising the performance of tailored porous structures in many other applications, such as heat exchangers or filters, with a large potential impact on capital cost, operating cost, and manufacturing sustainability.

Keywords: Net Shape, Powder Metallurgy, Pressure Sintering, SPS, FAST, HIP, Additive Manufacturing, L-PBF, Hydrogen Electrolysis, Bipolar plate, Porous Transport layer, Titanium, Sponge, HDH, Space holding, Dissolvable spacer, Salt, Sodium Chloride, Sodium Aluminate

1. The use of titanium within hydrogen electrolysers

In recent years governments across the world have committed to developing a low carbon hydrogen economy to reduce global dependence on fossil-fuels and enable wider geo-political energy security [1]. The vast majority of hydrogen sold today is extracted from fossil fuels; a chemical process which currently emits roughly the same amount of CO_2 into the atmosphere as the entire aviation sector [2]. It's therefore vital that the industry rapidly pivots towards hydrogen production which creates no harmful emissions. The clearest choice is so called "green hydrogen", in which hydrogen gas is extracted from water via electrolysis, powered using only renewable energy sources. A key metric that will determine the economic viability of switching to green hydrogen power in the coming decades is the Levelised Cost of Hydrogen (LCOH), which indicates how much it costs to produce 1 kg of Hydrogen, taking into account both the infrastructure capital cost and equipment operating costs involved.

Given the rapid pace of research and investment in this area, there are many competing electrolyser technologies being developed to minimise LCOH. However, a common theme amongst most designs is the need for tailored porous structures that optimise hydrogen extraction and can survive many years of operation.

Titanium is seen a s key enabling material for the porous transport layer (PTL) and bipolar plates used within Proton Exchange Membrane (PEM) hydrogen electrolysers, as well as some high-power PEM fuel cells. The function of a PTL is shown schematically in Figure 1, reproduced with permission from [3]. This is due to its unique balance of corrosion resistant properties (under low pH and high voltage anodic conditions) and relatively low material/processing cost vs. precious metal alternatives such as platinum.
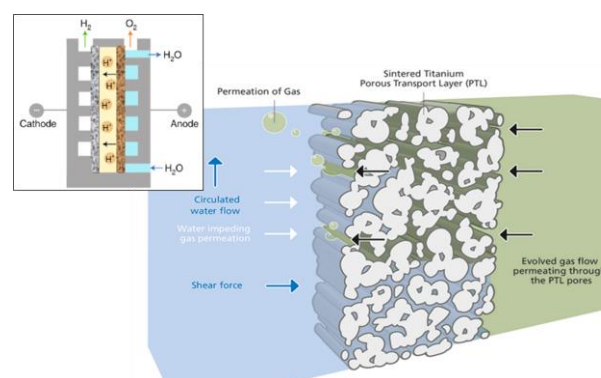
Figure 1. Schematic diagrams of; [Inset] an operating Proton Exchange Membrane Water Electrolyser (PEM-WE) cell; [Main image] the conflicting flow path of water into and oxygen bubbles out of the titanium PTL on the "oxygen evolution reaction" (anodic) side.

In previously published work [4, 5] the authors have reported new net-shape manufacturing routes for the creation of bipolar plates with integrated PTLs using recycled "low embodied carbon" titanium waste streams

and innovative dissolvable salt space-holders. This proved the capability of sodium chloride (NaCl) "table salt" to act as an effective space holder within both commercial purity Titanium (CP-Ti) and the workhorse titanium alloy Ti-6Al-4V (Ti-64) after pressure sintering.

This included the investigation of Powder Hot Isostatic Pressing (P-HIP) for processing a range of titanium waste stream powder materials at around 750°C and 35MPa pressure for 2-4 hours. The relatively low consolidation temperature was chosen due to the melting point of NaCl table salt being a little over 800°C.

An alternative approach was also evaluated using the Spark Plasma Sintering (SPS), also referred to as Field Assisted Sintering Technology (FAST), equipment located at the Henry Royce Institute in Sheffield University. This work proved that similar structures could also be produced under a temperature of 750°C and 35MPa pressure, however much faster processing was possible due to heating the samples via electrical current applied directly to the powder materials within the conductive graphite die. As a result, a cycle with only 15 minutes dwell time, rather than 2-4 hours was needed. The Joule heating effect not only heats up the powder faster than within a conventional HIP (which uses heating elements to warm inert gas within a pressurised furnace), but it also localises heat at the contact points between powder particles and speeds up local diffusion bonding mechanisms. The drawbacks relative to HIP are the limited size and complexity of graphite dies, as well as the fact that pressure is only applied uniaxially, rather than isostatic compression being applied in all directions.

Using the SPS/FAST system, and innovative NaCl salt-based space holding inserts, the MTC was able to produce complex titanium bipolar plates with an intricate internal flow field channel and integrated porous transport layer, as shown in Figure 2. These demonstrators were used to showcase the potential of this new manufacturing route in reducing both the capital cost (CapEx) and operating efficiency cost (OpEx) of a large and high performance PEM electrolyser stack.

In addition, low energy intensity powder materials, including both "recycled" hydride-de-hydride (HDH) Ti-6Al-4V and as-Kroll extracted titanium sponge fines (CP-Ti sponge) were evaluated and proven to consolidate effectively. The aim was to show that alternative "circular economy" methods were possible for processing titanium into complex hydrogen electrolyser components at a viable cost with sustainability benefits.
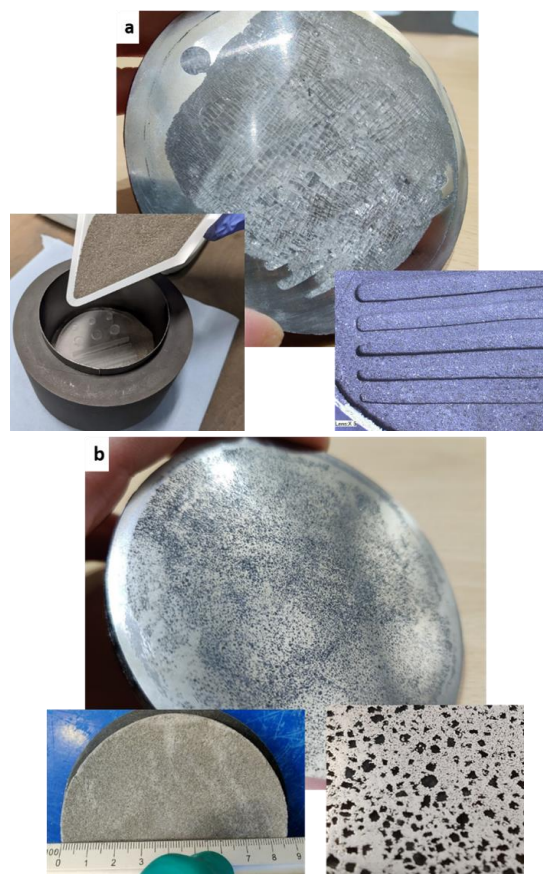
Figure 2. Photos from [3] of the SPS/FAST process used to manufacture titanium plates with: (a) solid NaCl salt inserts that can form cavities and channels, (b) pre-compacted inserts of CP-Ti sponge blended 50:50 with NaCl salt granules, that can form integrated open porous sections.

In the work presented here, the authors have taken the research further and evaluated a range of unconventional additive, subtractive, and net-shape manufacturing routes focused on creating graded porous structures. Conventional sintered powder or woven wire titanium PTLs have a very basic porous structure. By instead designing tailored porosity across the PTL a significant improvement in the performance of electrolyser cells could be achieved. This is firstly because you can control the flow of water into the PTL and evolved oxygen bubbles back out of the porous network (as shown in Figure 1), and secondly because you can have a significantly finer pore size with more even metallic titanium electrode contact with the catalyst/membrane where the water splitting reaction occurs.

2. Graded porous structures via net-shape consolidation with dissolvable salt space-holders

Conventional porous metallic sheets used in hydrogen electrolyser cells/stacks are either produced from woven wire mesh, or via partial sintering of powders. The semi-sintered powder process creates fully interconnected pores, but narrow convex channels and a

relatively small surface area compared to the much more open concave porous cavities created by the dissolvable space holder method being investigated in this work. Concave porosity potentially creates a more tortuous path for fluid flow through the structure (Figure 3), and a greater surface area for electrolysis reactions to occur. In addition, non-spherical space holders, such as needles or flakes, could be used to further tailor fluid flow through the porous structure and optimise properties for the desired application.
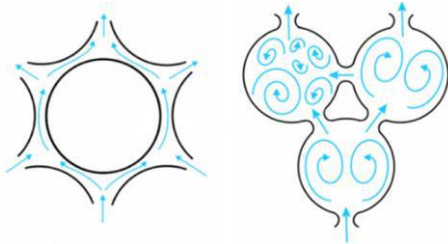
Figure 3. Comparison of convex pore surface in conventional semi-sintered powder vs. more concave pore surfaces theoretically produced by removable space-holders. Arrows show the influence on fluid flow.

The primary aim of this study was to prove the ability to tailor the pore size produced in fully consolidated powder parts simply by modifying the salt granule size in successive layers of powder. The second aim was to trial the use of higher melting point ionic salts which are also water soluble. The prime candidate was Sodium Aluminate ($NaAl_2O_3$) which is relatively low cost and non-hazardous but has a melting point of 1600°C (compared to 800°C for NaCl). This means it is potentially compatible with sintering of most major engineering alloys, such as steels and nickel superalloys which are typically powder consolidated between roughly 1000-1400°C. In terms of opportunities to improve the powder metallurgy of titanium, it was decided to repeat the previous HIP and SPS/FAST trials using Ti-64 plus NaCl salt, but this time using Sodium Aluminate salt and a higher temperature sintering cycle of 920°C. This temperature sits just below the beta transus allotropic phase transformation temperature for Ti-64 and is typically used to maximise the consolidation of powder without significant microstructural alteration.

As shown in Figure 4, this work successfully showed that Sodium Aluminate was able to act as a space-holder material under these processing conditions and a graded porous structure and internal cavity was created within a fully dense Ti-64 component. However, it was also observed that a chemical reaction occurred between the sodium aluminate salt and the titanium metal upon exposure to air. The precise chemistry of this reaction has not been fully determined, but it is likely that rapid oxidation is occurring, potentially accelerated by exposure to relatively high atmospheric humidity and the

very large surface area of intimate contact between the two materials. To halt the reaction the cross-sectioned HIP canister was submerged in an ultrasonic flowing water bath for 1 hour, which successfully removed all of the salt and halted any further corrosion. The same issue was observed after SPS/FAST consolidation of blended Ti-64 and $NaAl_2O_3$, therefore for the remainder of the experimental work it was decided to focus on optimisation of titanium porous structures using NaCl space-holders only.
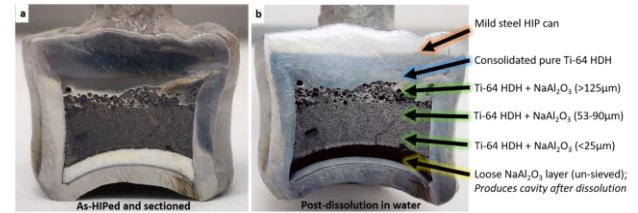
Figure 4. Use of sodium aluminate salt to produce a graded porous structure within a fully HIP consolidated Ti-6Al-4V HDH powder Ø20mm sample; (a) HIP canister as cross-sectioned, (b) after dissolution in an ultrasonic water bath to fully dissolve the salt.

In the next phase of work larger Ø80mm discs were produced with a central porous structure region of Ø65mm. The key stages of the manual manufacturing process are outlined in Figure 5. All powders were blended 50:50 Ti-64 to NaCl, and the batches with different sieved NaCl granule sizes were layered carefully on top of each other within the central porous section of the PTL demonstration plate. As shown by the post-SPS/FAST cross section in Figure 6, distinct layers with different porosity size were produced.

Figure 5. Clockwise from top left: SPS/FAST Ø80mm die filling with central Ø65mm tube, pure Ti-64 rim and central blended Ti-64 + NaCl sections after filling, the consolidated part encased in conductive graphite paper, the final part after the graphite paper is removed.
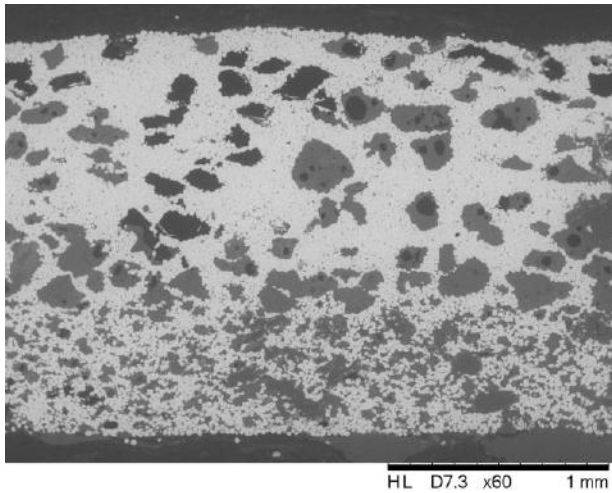
Figure 6. A representative cross-section through an as-SPS/FAST processed porous discs produced by the manual filling method in Fig.6.

The key factor enabling open porosity, consisting of a fully interconnected network of both fully bonded metal and free space, is the ratio of salt granules to titanium powder in order to ensure all salt particles remain in contact with each other and the surface. If this is achieved, then all of the salt can be successfully dissolved away during post processing.

One clear outcome of the work shown above is that manual powder handling produces inconsistent results, both in terms of the geometric dimensions of the internal porous part, and the consistency of the open porous structure itself. Rather than undertake a number of experimental iterations to further optimise the manual powder filling and consolidation process, it was decided to pivot towards investigation of automated powder handling processes. There are a number of techniques under commercial development which are capable of directly filling a HIP canister or SPS/FAST die with multiple powder materials to create complex components.

The authors have utilised a multi-material powder printing system developed by Grid-Logic Inc., who have collaborated in this research. The process enables the simultaneous printing of titanium and salt powder, as well as pre-blended mixtures, directly into a HIP canister at tap density. A non-sintering ceramic retaining media can also be printed between the part and the HIP canister in order to form more complex part geometries. For example, in Figure 7 a cylindrical disc of CP-Ti (with an NaCl plus CP-Ti core) is being printed within a cuboidal steel HIP canister. These ceramic particles transfer isostatic load during HIP, but do not diffusion bond and therefore can simply be shaken out of the canister post-HIP to reveal the consolidated part.
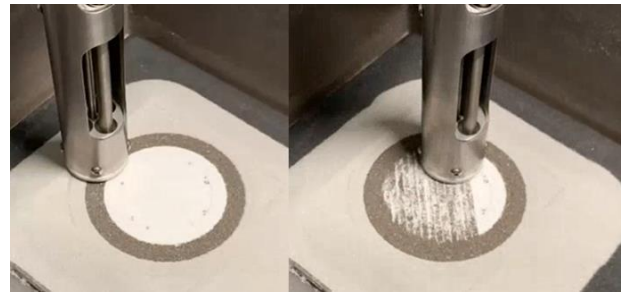
Figure 7. Photos from initial multi-material HIP can powder printing trials undertaken at Grid-Logic Inc. USA using CP-Ti sponge and NaCl salt enclosed within a powder ceramic retaining media.

Several printed trial components have been successfully HIP consolidated and the NaCl salt removed. Further analysis is required to fully characterise the potential of this technique to improve upon the manual powder handling methods trialled previously, but the initial work indicates it will yield significantly more consistent components that are suitable for direct use within hydrogen electrolyser applications and beyond.

3. Graded porous structures via a Parameter Controlled Additive Manufacturing method

Additive Manufacturing (AM) is known for its ability to produce geometrically complex structures, and a significant amount of research has been conducted into the use of AM to produce porous structures. Three main methods have been identified and each has unique advantages and limitations in terms of the control in size, shape and overall porosity which can be achieved:

1. The use of fillers or pore former materials is similar to the net-shape dissolvable salt space-holder approach described previously. The benefit of this approach is that very fine pores (~2µm in size) can be produced and there is good control over the overall level of porosity within the structure (35-80% porosity depending on additive material used and manufacturing method) [6, 7, 8].

2. Structural control refers to standard operation of AM equipment incorporate porous structures into the computer aided design (CAD) geometry. Pore size is limited as un-melted powder must be extracted from the build.

3. Parameter control refers to intentionally inducing solidification porosity within the material through manipulation of the AM process parameters. This has been the focus of the work undertaken in this report.

The development of process parameters to control defects and density during titanium Laser Powder Bed Fusion (L-PBF) is well understood, but this typically

focusses on eliminating porosity and maximising density. However, the reverse can also be achieved, whereby laser power, scan speed or spacing is manipulated to induce keyhole pores or lack of fusion features. This can be achieved either using continuous wave or modulated/ pulsed lasers, but the latter offers greater opportunity to generate porous structures as the distance between circular melt pools can be separated out to induce deliberate solidification porosity features.

This method is capable of producing finer pores than structural control, without the need for additives to the feedstock. It is possible to produce graded structures with this methodology; typically, pore sizes less than 300µm with porosities between 0 and 55% are achievable. However, there is an unknown level of both repeatability, and it may be difficult to control the shape and distribution of pores using this method. As can be seen in Figure 8, there is a threshold for overall porosity where the structure becomes too fragile and poor buildability or build failure occurs.
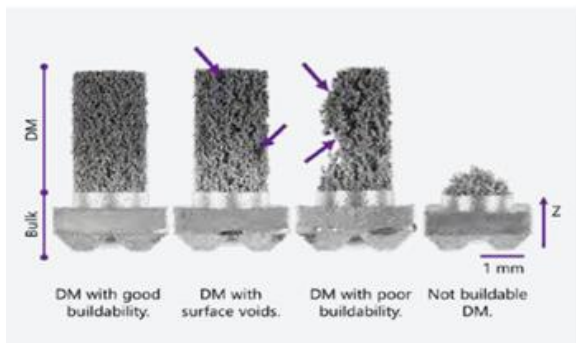
Figure 8. Porous structures showing increased porosity (left to right) with reduced buildability. From Albert, 2022 [9].

A review of laser process parameters was conducted looking at literature values used for the generation of porous structures as well as the default, fully dense parameters for the Renishaw 500Q system selected to process Ti-64 in this work. The standard parameters for this machine use a layer thickness of 60 µm. However, it was decided 30 µm layer thickness would provide greater ability to produce smaller pore sizes, and this was highlighted in the porous parameters from the literature review. As such, it was kept constant in the Design of Experiment (DoE). The target porosity values for this work were 20-50% with a target pore size below 100 µm.

A 4-factor, 2-level full factorial DoE (DoE 1) was developed (see Table 1). A centre point, and three repeats of each parameter were included as per MTC best practice on AM process development (51 samples total), and the location of the samples were randomised to remove the effects of build location. All parameters not detailed, were kept consistent to the default process parameters.

Table 1: Parameter Controlled AM DoE 1 & 2 Variables and Levels

Variable	DoE 1		DoE 2	
	Low	High	Low	High
Laser Power (W)	100	200	100	150
Point Distance (µm)	75	250	150	200
Hatch Spacing (µm)	75	250	150	200
Exposure Time (µs)	30	100	50	70

Following, the completion of the DoE 1 build, nine samples (three parameters) were identified as failing to build (see Figure 9). Metallurgical evaluation was completed on 12 samples (4 down-selected parameters), and pore evaluation conducted via image analysis. Figure 10 shows the pore size and shape indicator data, along with cross sectioned optical micrographs, of the largest and smallest pore sizes achieved. It was seen that pore size decreases as metallurgical density increases. Typically, circularity and roundness values were between 0.6 and 0.8 for samples measured and there was no trend seen. Additionally, there was no correlation seen between energy density and pore size.

DoE 1 analysis showed that all parameters affected the density of the component, however, point distance and exposure time had the greatest effect. This suggests that the structures were failing to build where adjacent melt pools were either too small (exposure time too small) or to widely spaced (point distance too large). Most importantly, it was shown that pore sizes below 50 µm are achievable with this manufacturing method.
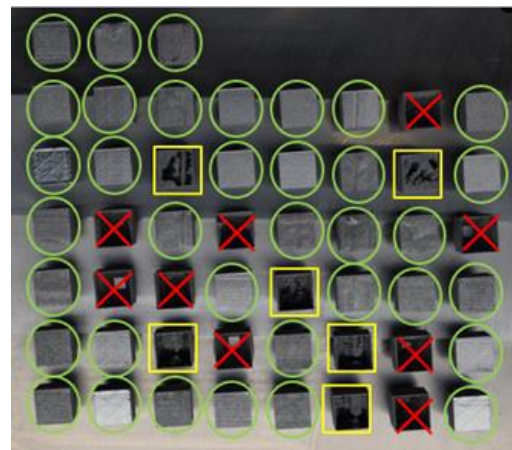
Figure 9. Build Photo: DoE 1 (green parts built completely, yellow parts incomplete build, red parts failed to build at all)

Figure 10 Optical micrographs from cross-sectioned DoE 1 samples with the largest and smallest measured pore sizes.

DoE 2 was planned to target greater porosity and identify the achievable limits of the methodology. It was clear from DoE 1, that energy densities less than 150 J/mm3 would be required to achieve this, but the ranges for the variables were narrowed in an attempt to reduce build failures. A two-block approach with powers of 100 W and 150 W was taken with a 3 factor, 2 level, full-factorial DoE; the variables and levels can be se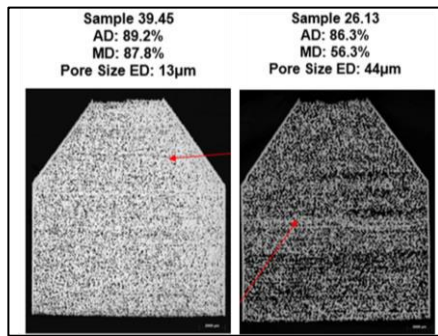en in Table 1. Parts with energy density less than 42 J/mm3 failed to build. Parts with energy densities between 65 and 98 J/mm3 built incompletely, and with 77-155 J/mm3 built completely. Therefore, DoE 2 clearly showed that exposure time is the dominant factor controlling the density of porous structures, particularly at higher levels of porosity. Parts typically failed to build at densities below 65%.

Using the optimised printing conditions from DoE 2 demonstration parts were manufactured. These were similar to the net-shape PTL component, however this time a solid Ti-64 ring was printed at the edge of the disc, followed by an inner medium density/ small pore size ring and a central low density/ large pore region. At such low density the parts are fragile, so thin solid walls were added to provide strength to the structure when scaling up from the Ø15mm DoE samples to the Ø65mm porous sections produced here. However, Figure 11 shows that a part with clearly graded porosity can be produced using the methodology developed in this work.
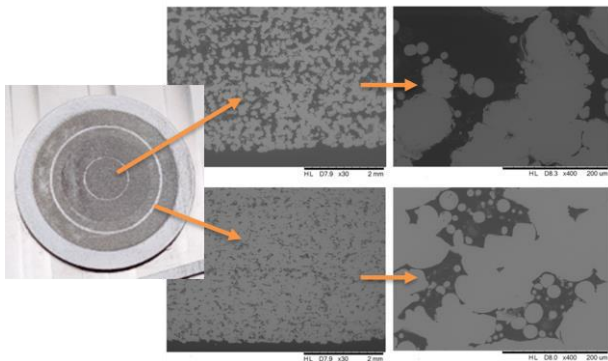
Figure 11. Build Photo: L-PBF Ti-64 graded PTL demonstrators and optical micrographs of cross-sections in the centre and inner ring.

4. Conclusion

This study has investigated innovative net-shape and additive manufacturing processes which show promise for producing highly tailored titanium porous structures. These have significant potential to enable new, more efficient, and potentially less costly designs of hydrogen electrolyser and fuel cell to be developed. Further work is required to apply each of them to the fabrication of specific devices, and undertake detailed business models and Life Cycle Assessment (LCA) at production scale to prove their worthiness within the burgeoning hydrogen value chain and beyond.

5. Acknowledgements

6. References

1. International Energy Agency, Global Hydrogen Review 2022, *IEA Publications*, September 2022.
2. International Energy Agency, The Future of Hydrogen, *IEA Publications*, June 2019.
3. J. Garcia-Navarro et al., Understanding the Role of Water Flow and the Porous Transport Layer on the Performance of Proton Exchange Membrane Water Electrolyzers, *ACS Sustainable Chemistry & Engineering, January* (2019). Copyright 2019 American Chemical Society. Reprinted with permission.
4. I. Berment-Parr et al., Dissolvable HIP space-holders enabling more cost effective and sustainable manufacture of hydrogen electrolyzers, *International HIP22 Conference, Columbus, OH, USA* (2022).
5. I. Berment-Parr et al., Dissolvable Salt Inserts Enabling Complex And Porous Titanium Structures To Be Consolidated From Powder At Low Cost, *World PM 2022 Congress, Lyon, France* (2022).
6. A. Jakus et al., Water-Soluble Salt Particle Containing Compositions and Porous Materials Made Therefrom, *United States of America Patent WO 2019/10853 A1*, 06 June 2019
7. Y. Shen, D. Gu and P. Wu, Development of porous 316L stainless steel with controllable microcellular features using selective laser melting, *Materials Science and Technology*, vol. 24, no. 12, pp. 1501-1505 (2008)
8. Y. Man et al., A review on porous ceramics with hierarchical pore structure by 3D printing- based combined route, *Journal of Asian Ceramic Societies*, vol. 9, no. 4, pp. 1377-1389 (2021)
9. J. Albert et al., Investigation on Process Stability and Part Positioning Influence on the Relative Density of Designed Materials via Laser-Based Powder Bed Fusion of Metals on a Multi-Laser Machine, *Advanced Engineering Materials*, vol. 24 (2022)

TITANIUM / TITANIUM DIBORIDE COMPOSITE FIELD-ASSISTED SINTERING TECHNOLOGY (FAST) PROCESS MAPPING FOR POTENTIAL ARMOUR PRODUCTION

James Pepper, Simon Graham, Martin Jackson

Department of Material Science and Engineering, The University of Sheffield, Mappin Street, Sheffield, S1 3JD, UK.

There is an increasing use of armour piercing projectiles globally and these constitute a significant threat. This threat is most eminent for wearers of body armour and to lightly armoured combat vehicles. As part of the solution to this problem, new generations of lightweight armour designs are under development. One promising possibility has been found to be the use of functionally graded materials as armour materials. In such materials, the high hardness of ceramics is combined with the ductility of metals; in our study the system of Ti-3Al-2.5V–TiB_2 was used. Fully dense 20 mm and 80 mm diameter Ti-3Al-2.5V discs were produced using Field Assisted Sintering Technology (FAST) with stepped functional grading - using 0, 6, and 9 wt.% TiB_2 - for prospective application in armour plating. The in-situ generation of a significant quantity of resistant ceramic TiB needles was confirmed in the FAST billets, and their relationship with the FAST-processing temperature and dwell time was mapped between 900°C and 1400°C for up to 6 hours. The microhardness of said samples were measured and recorded, demonstrating the impact of this ceramic inclusion.

Keywords: FAST, SPS, Mixed Metal Composites, TiB_2, Process Mapping, Ballistic Materials.

1. Introduction

Increasing threats from the rising use of small calibre armour piercing projectiles poses a great danger to both lightly armoured vehicles and personnel in global combat zones. Between this and the advancement in military technologies, such as explosives, the development of newer light armour has risen to a position of higher demand. These new materials must have high hardness, fracture toughness, elastic modulus, as well as the highly desirable multi hit capacity. Meaning the material must be able to withstand multiple impacts without too great of a loss in these important properties.

TiB_2 as a ceramic offers most of the required properties as an armour material, however full consolidation of this material requires long dwell times at sintering temperatures of approximately 2000°C. These conditions commonly cause melting in their combined metal partner material, or at least adversely affect the mechanical properties from microstructural effects and reaction zones at these temperatures. This is especially true for titanium which experiences large grain growth above the β transus temperature of ~1000°C [1]. This has previously been attempted as a positive effect in work by Gupta et al. [2]. Titanium has been selected regardless of this however, as it provides significant fracture toughness to the system and has a similar density and coefficient of thermal expansion to TiB_2, and is therefore, thermomechanically compatible. It additionally provides more titanium for the ceramic to react with to form the desired TiB needles, further strengthening the system.

We consolidated our billets using Field Assisted Sintering Technology (FAST) to demonstrate FAST's capability to generate unique microstructural solutions to real world issues. This technique is a low voltage, DC activated sintering technique using uniaxial pressure together with resistive heating, allowing it to consolidate a wide variety of materials. In addition, FAST performs this consolidation many times faster than other alternative techniques, such as Hot Isostatic Pressing (HIP) and is capable of high heating rates above 200°C/min in our equipment. Another benefit of the technique is the ability to combine similar and dissimilar materials in a single step, here we take advantage of this to layer specific depths of the three TiB_2 concentrations for a potential purpose as an armour material. We have focused this work on this TiB_2 [3] and titanium system as a type of Metal Matrix Composite (MMC) armour ceramic in the form of a Functionally Graded Material (FGMs).

A FGM may in this case be visualised as a stack of these MMCs with varying concentrations of ceramic inclusion. The differing mechanical properties of each layer may be decided upon in advance to create a bulk performance suited to the needs of the task. In this case the high hardness of the ceramic elements may provide impact protection on the surface, while the relative ductility of the Ti-3Al-2.5V alloy would allow for the absorption of the incoming energy and material on the rear face. This has progressed in our work using previously cold milled powder allowing the combining of these elements on a much more refined scale, allowing for a homogeneous structure to be formed in a single sintering step akin to the previous work [4]. In addition, we are using only low percentage ceramic inclusions with the intent of reducing fabrication difficulties from high temperature requirements and promoting the growth of TiB needles through the TiB_2 + titanium reaction in situ [5] to increase fracture toughness resistance. The growth of such needles has been demonstrated before using an

annealing process, over a period of up to 50 hours [6-7]. They possess no obvious preferential orientation from the FAST process and a hardness multiple times that of the underlying titanium substrate. As such it is expected that their presence will provide several additional barriers and hard/soft interfaces for the projectile and resulting cracks to encounter, further increasing the ballistic performance.

2. Methods

The microstructure and morphology of the initial hydride-dehydride (HDH) Ti-3Al-2.5V powder which was cold milled with 6 wt.% of TiB_2 is shown in figure 1. A portion of the particles have been very well seeded (figure 1B) while other HDH particles seem to be almost entirely untouched (figure 1A). It is believed that this is due to trapping of the TiB_2 between the titanium powders via a cold welding mechanism during the milling process. An additional blend with 9 wt.% was also created to provide a harder surface for future testing and a comparison between different concentration layers and their bond.

These samples were initially laid up in 20 mm discs split into two equal layers, pressed to 35 MPa and heated at a rate of 100°C/min to dwell temperature in the FCT Systeme GmbH Spark Plasma Sintering Furnace type HP D 25. A range of temperatures (900, 1000, 1200, 1300, 1400°C) and times (10 min, 30 min, 1 hr, 2 hrs, 6hrs) for this dwell period were tested where deemed productive for additional consolidation and needle growth. These were then slow cooled under vacuum before extraction and preparation for microscopy and SEM imaging.

An 80 mm sample was then also produced under the previously determined conditions from this process mapping for needle growth using the same sintering process. However this had been produced with five layers (9 / 6 / 0 / 6 / 9 wt. %), see figure 6, to test for any potential directionality in the process from the flow of current, as well as testing the scalability of the material system to the limits of this machine.

The hardnesses of the samples were then finally tested using the Vickers method at a pressing force of 1 kgf in each of the layers as well as each of the bonding zones. There were several repeats for each of these tests to average out the presence of differing quantities of needles and TiB in each. Ranges were presented with the data to represent this variability.
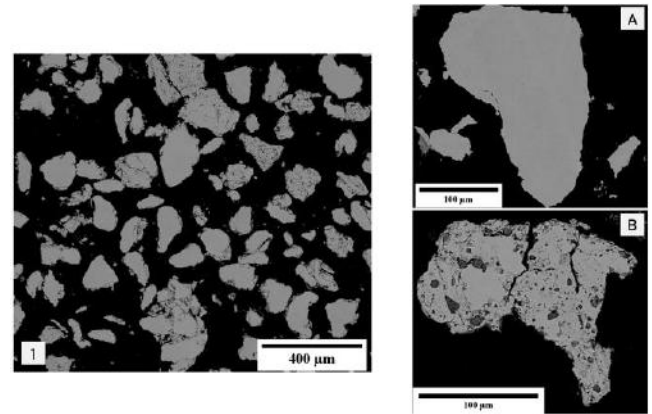
Figure 1: BSE image of (1) the HDH Ti-3Al-2.5V with 6 wt.% TiB_2 milled powder; (A) HDH Ti-3Al-2.5V particle unseeded and; (B) HDH Ti-3Al-2.5V particle seeded with TiB_2.

3. Results

3.1. TiB Needle Production

Initial samples were processed according to previous work by Singh et al. at 1200°C for 2 hrs to demonstrate the materials would in fact create the needles under FAST conditions. Figure 2 shows an example of these needles grown in situ during the sintering process of "significant length" at differing magnifications. Significant length here refers to needles longer than 20 μm in length as the milled TiB_2 powder would have needed to react and grow to achieve this scale. It may also be noted that these are only the needles which fell in the plane of the cut used for sample prep and many of the shorter examples are likely at an angle to this plane, thus not showing their full scale.
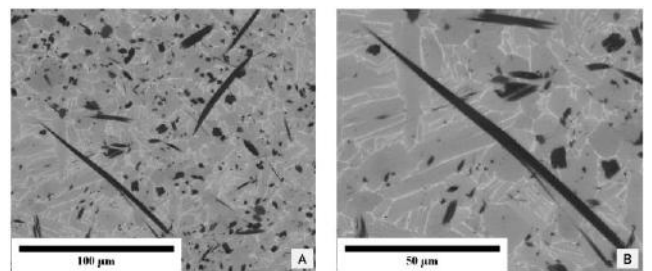
Figure 2: (A) BSE image of the 6 wt. % TiB_2 milled powder with the HDH Ti-3Al-2.5V alloy close to the boundary layer, FAST processed at 1200°C for 2 hrs. (B) Higher magnification BSE image of the very apparent TiB needle growth with maximum lengths between 50 and 100 μm.

Examples of needles were observed under BSE imaging at these conditions; however, it is important to sample the surrounding temperatures to generate a full process map. This map will help with both deciding the most efficient conditions to produce a certain microstructure without waste energy, and to analyse thermal history of samples in future.

3.2. Extended Process Mapping
3.2.1. Full Range

These samples were made from 900°C 10 min to 1400°C for 6 hrs at 20 mm diameter, and imaged using SEM. Average needle length, if any were produced, and visual determinations of needle count were recorded within a fixed area.
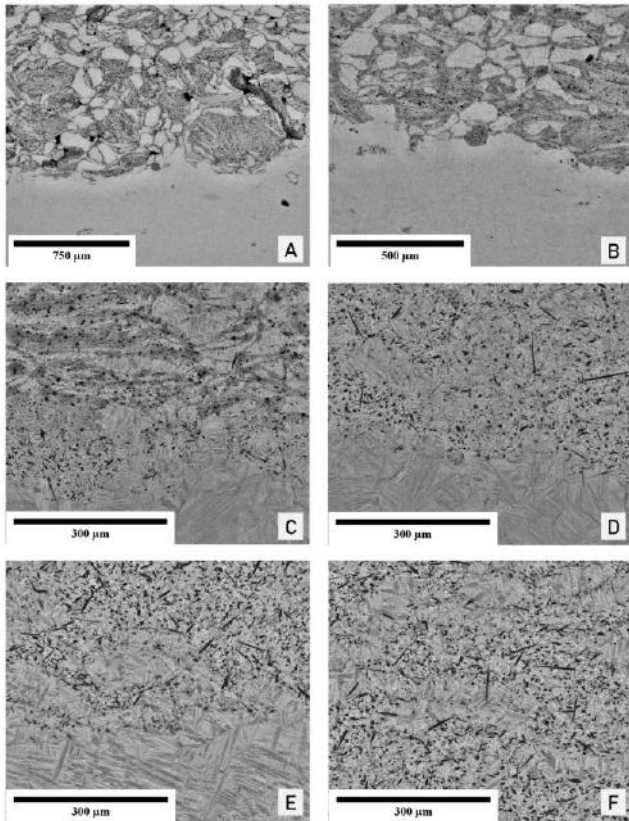
Figure 3: A-E: BSE images of the 0-6 wt.% TiB_2 boundary layer with increasing energy conditions (A-900°C 10 min / B-1000°C 10 min / C-1200°C 30 min / D-1200°C 60 min / E-1400°C 60 min) . F shows the boundary between the 6-9 wt.% TiB_2 boundary for the 1400°C 6 hr condition.

The lack of needle growth at 900°C was expected as the lowest temperature from literature we have noted the TiB reaction at is ~1050°C [8] but we also saw no needle production in at 1000°C (B) though with a slight increase in homogeneity. C shows the first production of needles of significant (>20 µm) size, primarily on the boundary with the Ti-3Al-2.5V layer, likely due to the more abundantly available titanium to fuel the TiB_2 reaction. However, this seems to be a thin layer, approximately 100 µm deep and much of the inhomogeneity remains with discolouration in the MMC layer. In D we can see the end of this region of clearly bounded layers in the MMC material, as well as the first needles of ~100 µm length. These needle growths also penetrated far deeper into the material as desired. Figure 3 E and F both show notable increases again in both needle density and average length, though it may be noted

that this is a significant increase in dwell time and temperature and this level of increase may be considered a diminishing return at this point with very little unreacted TiB_2 remaining to form or grow additional needles. Overall, the figures demonstrate the increasing homogeneity and needle growth, though at a diminishing rate, as the energy of the system increases. This is demonstrated more clearly by the quantified length and number of needles plotted in figure 4.

It may be noted that the count, whilst dependent on the image in question, seems to plateau earlier than the size, suggesting that almost all of the TiB_2 in the samples has reacted to form TiB at 1300°C 1 hr, but the increase in energy can allow for further growth and penetration of these needles. Small enclaves of uninfused titanium alloy remain even at these high energy processing conditions, as expected when comparing to the powder images from Figure 1, and these are potential areas for further homogenisation. However, we believe that increasing the processing temperature much further leads to potential risk of partial melting at the alloys melting temperature of 1700°C with localised hot spots or contaminants from the milling process. It is also possible to increase the dwell time further, but the energy intense nature of this approach would potentially make it impractical for many uses.
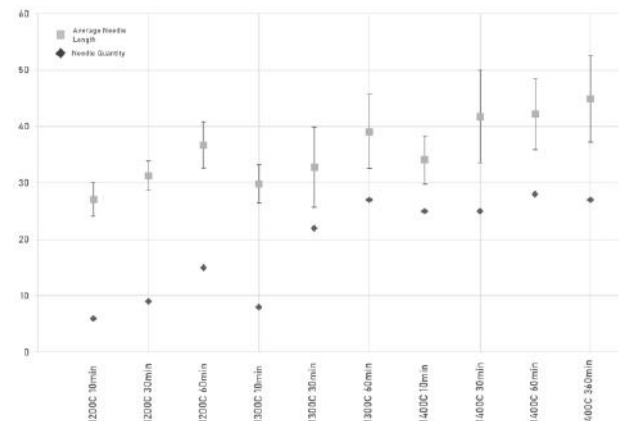
Figure 4: Characterisation of Needle Growth displayed graphically for our initial process mapping of the Ti-3Al-2.5V + TiB_2 system, demonstrating the increase in these features with additional applied energy, and subsequent plateauing of said values.

The needle production can be seen to increase consistently past the point at which the energy available is sufficient to start the reaction but slows to plateau at around 1400°C, above 30 min in dwell time. Previous efforts with higher concentrations of TiB_2 have shown increasing results for longer dwell times however, aside from the energy concerns mentioned above, this is impractical with the equipment we have access to and excessive as we have already reached a relative peak in

needle production for these concentrations of ceramic inclusion.

3.2.2. Microhardness Testing

Looking at the impact of this visual difference on the hardness at various points was then carried out. The results are shown in figure 5 and seem to suggest little difference within the layers themselves with respect to hardness. There is a seeming increase in the value when examining the bond between the two layers, however when examining the data further, we can see that this is dependent on the locations measured. The hardness increases with the increased inclusion of the TiB2 ceramic and the temperature impacts this minimally. While the variance in the values is much more strongly tied to this variable. The standard deviation of the points relates to this variation and the colour variation, from boron inclusion, in the micrographs, seen in figure 3 A-C. The lower temperature samples at 900°C show high variation at all points where the ceramic is present, while with enough energy the 1200°C sample enables sufficient diffusion to even out the distribution and thus the resulting hardness. And the 1400°C sample allows for an improvement even within the bond region.

Figure 5: Grouped bar plots of the microhardness measured from 3 Ti-3Al-2.5V + 0-6 wt.% TiB$_2$ samples at increasing temperatures for the same 10 min of dwell time.

3.3. Scaled Sample Profiling

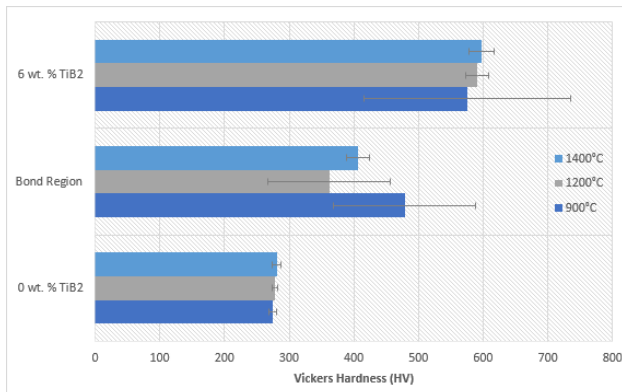Once the process had been mapped at a smaller 20 mm scale, an 80 mm diameter sample was produced on the same machine at parameters which had been determined to produce reasonable needle growth to check feasibility of scale, 1200°C for 10 min. In addition, this sample was laid up as a true functionally graded material, as visible in figure 6, with horizontal symmetry in its layers to check for any directionality in the process to be accounted for in future. The 9 wt.% layer is external as for ballistic purposes this would need to be the attack face for future work.
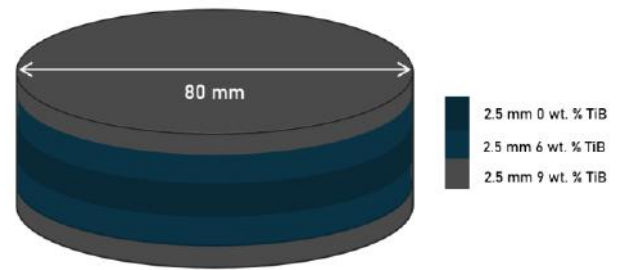
Figure 6: Diagram schematic of the as sintered layers of our FGM Ti-3Al-2.5V + TiB$_2$ system powders in this 80 mm diameter sample with a final height of 12.5mm. Processed at 1200°C for 10 min and later an identical sample processed at 1300°C for 1 hour.

These processing conditions were chosen with the explosive grain growth of titanium alloys in mind once the allotropic tranus temperature (β transus) is reached. The intent was to find conditions at which the needles could be grown successfully and homogeneously whilst retaining a reasonably super transus grain structure for the pure titanium alloy layer to retain desired properties such as ductility and strength. However, initial trials with this design demonstrated the microstructure of samples processed at significantly lower temperatures with very little needle growth and very anisotropic distribution in the ceramic doped layers visible in figure 7 A-B.

3.3.1. Improved 80 mm Sample

With this knowledge of an increased energy requirement to achieve the same microstructural results with larger volume samples we selected a condition further along the energy scale of our process mapping. An additional sample was then sintered at 1300°C for 1 hour to ensure the desired needle growth occurred. This adjustment dramatically improved the microstructure at the boundary with the titanium alloy and there was also a significant increase in the isotropic nature of the layers of higher concentration on the faces of the sample. These are displayed in figure 7 C-D and provide strong suggestions that this technique may be used to produce materials within this system on a larger scale for real world applications. It may also be noted that no variation was noticed between either side of the layers, showing no directionality to this growth process or diffusion direction dependency on current flow during the sintering process.

Figure 7: A-B show the 80 mm microstructure in BSE images of the 0-6 wt.% TiB$_2$ boundary and 9 wt.% TiB$_2$ regions for the 1200°C 10 min sample respectively. Whilst C-D BSE images show the same regions for the sample produced at 1300°C for 1 hr.

3.3.2. Final Microhardness testing and implied Yield Strength
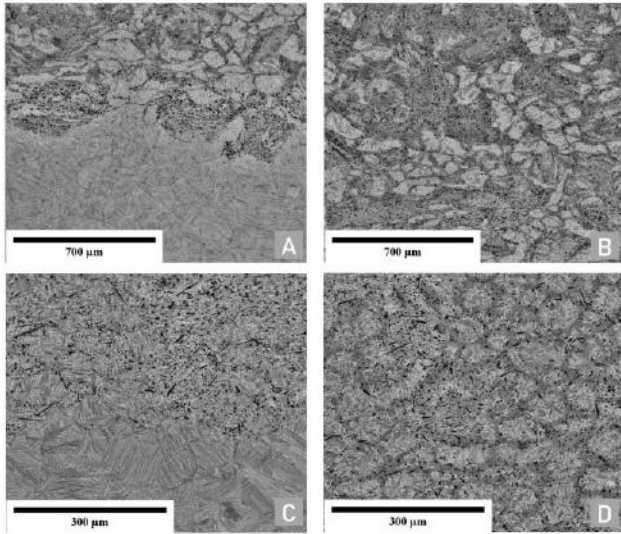
These samples were then once again tested using the microhardness indenter for quantitative comparison and further validation of the connection between variance in hardness and inhomogeneity in microstructure. The hardness reading this time were measured, not in a grid pattern within the layers as before, but in a diagonal line across the full height of the samples including all layers as an additional test of directionality for both consolidation and needle growth. These have then been displayed from edge to centre in such a way as to make both centre-edge transitions comparable.
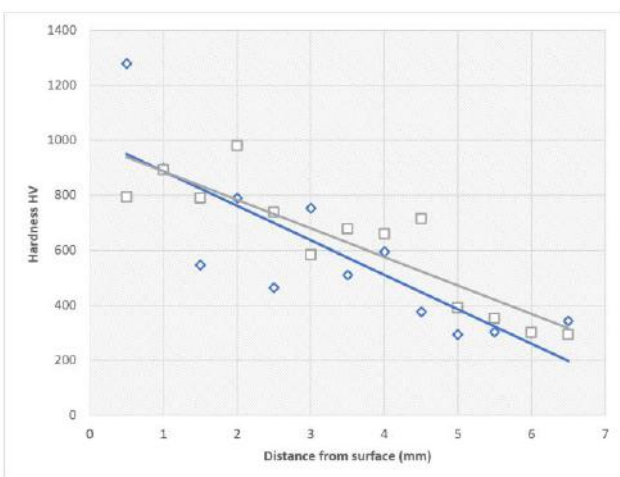

Figure 8: Graph demonstrating microhardness of the 1200°C 10 min sample from the hard 9 wt.% TiB$_2$ edge to the Ti-3Al-2.5V centre of the 80mm sample (figure 6).
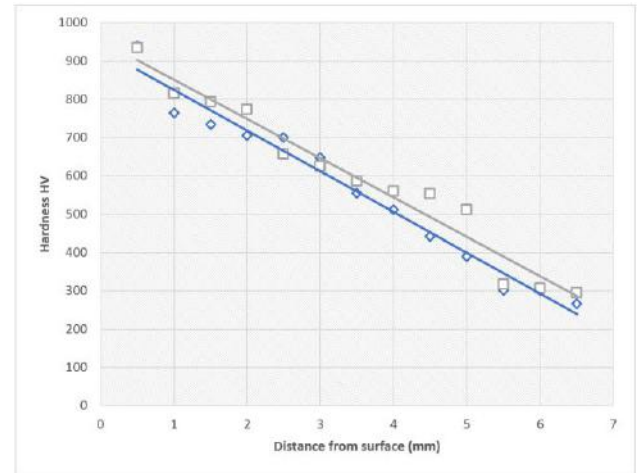
Figure 9: Graph demonstrating the microhardness for the 1300°C 1 hr sample from the hard 9 wt.% TiB$_2$ edge to the Ti-3Al-2.5V centre of the 80mm sample with a marked improvement in consistency from figure 8.

Figures 8 and 9 above clearly demonstrate the inhomogeneity from the microstructure impacting the properties, in this case, the microhardness (HV). As the indenter perceives unreacted, enriched regions of relatively soft titanium alloy or much harder TiB/TiB$_2$ this results in the high degree of variance noted here in the hardness results. There is a second point to note in these graphs also, that the diagonals were taken from as close to the centre of the sample as possible in both cases. This is important as the radial edges of both samples displayed an average hardness of ~10-30 HV lower for the ceramic doped layers at the edge of the samples compared to their centres. This is likely from some small thermal gradients within the samples over the 40 mm distance but could also be some degree of remaining variability inherent in an MMC system like this. More generally, these results are very impressive for only 9 wt.% TiB$_2$ inclusion given the hardness of the pure sintered TiB$_2$ system was found to be 2527 HV ± 50 HV when consolidated at above 2000°C in the same machine.

4. Discussion

These results show that, like in previous work, we have been able to create in situ growth of these TiB needles but with greater size and distribution than seen previously at these concentrations due to alterations to the processing conditions. Mapping these conditions has allowed us to find optimal processing routes and a larger scale 80mm sample has been successfully produced, imaged, and tested, demonstrating the scalability of generating this microstructure using FAST. The bonded regions between the 0 wt. %, 6 wt. %, and 9 wt. % regions has also demonstrated a very good level of bonding, allowing for the creation of functionally graded material parts with a reasonable homogeneity throughout each

layer. The hardness values also provide good insight into the great potential of this concept for ballistic success at low wt. % TiB$_2$ infusion through FAST.

Future scalability of the process to 250 mm is planned and will hopefully allow for further testing, ballistically or from machined coupons. However, it is predicted that the thermal gradients from scale up, seen on a small level at 80 mm, could have an impact on the performance as microstructures from lower temperatures are clearly different with reduced degrees of strength. This region responsible within the ceramic infused layers of discoloured material is chemically very similar under X-EDS and as is assumed to be caused by minor variations in diffused boron content or other inclusions from the milling process impacting the matrix.

5. Acknowledgements

6. References

1. Weston, N.S., Derguti, F., Tudball, A. et al. Spark plasma sintering of commercial and development titanium alloy powders. J Mater Sci 50, 4860–4878 (2015).
2. Gupta, Neha & Basu, Bikramjit & Prasad, V.V. & Vemuri, Madhu. (2012). Ballistic Studies on TiB2-Ti Functionally Graded Armor Ceramics. Defence Science Journal. 62. 382-389.
3. Schmidt, J., Boehling, M., Burkhardt, U. and Grin, Y., 2007. Preparation of titanium diboride TiB2 by spark plasma sintering at slow heating rate. Science and Technology of Advanced Materials, 8(5), p.376.
4. Singh, N., Edachery, V., Rajput, M. et al. Ti6Al7Nb–TiB nanocomposites for ortho-implant applications. Journal of Materials Research 37, 2525–2535 (2022).
5. Ma, F., Liu, P., Li, W. et al. The mechanical behavior dependence on the TiB whisker realignment during hot-working in titanium matrix composites. Sci Rep 6, 36126 (2016). https://doi.org/10.1038/srep36126
6. S Gorsse, D.B Miracle, Mechanical properties of Ti-6Al-4V/TiB composites with randomly oriented and aligned TiB reinforcements, Acta Materialia, Volume 51, Issue 9, 2003, Pages 2427-2442.
7. S Gorsse, J.P Chaminade, Y Le Petitcorps, In situ preparation of titanium base composites reinforced by TiB single crystals using a powder metallurgy technique, Composites Part A: Applied Science and Manufacturing, Volume 29, Issues 9–10, 1998, Pages 1229-1234
8. Abbas Sabahi Namini, Shaikh Asad Ali Dilawary, Amir Motallebzadeh, Mehdi Shahedi Asl, Effect of TiB2 addition on the elevated temperature tribological behaviour of spark plasma sintered Ti matrix composite, Composites Part B: Engineering, Volume 172, 2019, Pages 271-280.

DEVELOPMENTS IN TITANIUM PROCESSING AT CSIRO

Mark J. Styles[1], Peter C. King[1], Alejandro Vargas-Uscategui[1], Felix N. Lomo[1,2], Milan J. Patel[2], Ivan S. Cole[2], Robert Wilson[1], Kun Yang[1], Lyndsey L. Benson[1]

1 CSIRO Manufacturing, Gate 3 Normanby Road, Clayton, Victoria 3168, Australia.
2 School of Engineering, RMIT University, Melbourne, Victoria 3000, Australia.

The Commonwealth Scientific and Industrial Research Organisation (CSIRO), Australia's national science agency, has a long history of research and development across the titanium value chain. In recent years, CSIRO's Lab22 additive manufacturing centre has showcased the capabilities of advanced additive manufacturing technologies, facilitating research in collaboration with Australian universities and the adoption of technologies by industry. Lab22 is set to grow further in the next few years, with titanium processing playing a central role in this expansion.

This paper describes two examples of developments at CSIRO towards the goal of realising larger format additive manufacturing of titanium components. The first example describes fundamental studies of how Grade 2 titanium and titanium matrix composites deposit during cold spray additive manufacturing and the properties that can be obtained following heat treatment. In the second example, an update on scaling the TiWi process for producing titanium and titanium alloy wire from waste powder forms is presented with characterisation and modelling results.

Keywords: Cold spray, additive manufacturing, powder metallurgy, wire.

1. Additive manufacturing of titanium by cold spray

Cold spray is a solid-state deposition process that converts a powder feedstock (typically <45 µm) into a densified layer by accelerating particles towards a surface using a supersonic gas jet, typically comprised of high-purity N_2, He, or sometimes compressed air. Historically cold spray has been used for coatings and for repair of damaged components, however, over the last fifteen years, CSIRO has been developing techniques for additively manufacturing (AM) large, free-form objects by cold spray [1]. In the case of titanium, a chief advantage is the ability to produce low-oxygen deposits without enclosing the workpiece in an inert environment, which is costly and imposes restrictions on build volume.

A challenge, particularly with cold spraying of titanium, is the presence of porosity in the deposit. Ductile, dense metals such as copper experience sufficient particle deformation and flattening upon impact to create deposits with essentially no remaining porosity. In comparison, titanium is more resistant to deformation, particularly in its alloyed form. The following examples describe fundamental research performed towards understanding micro-structure-property relationships in cold sprayed titanium deposits, which is necessary to achieve the goal of producing large titanium components by this technique.

1.1. Microstructure of as-cold sprayed titanium

The microstructures produced by the high-velocity impact of titanium particles during cold spray were examined by transmission electron microscopy (TEM). A gas-atomised powder (TLS Technik, Bitterfeld, Germany) was chosen with a particle size distribution of d10 = 12.1 µm, d50 = 21.9 µm, d90 = 34.2 µm, measured by laser diffractometry. Samples were made using a Cold Gas Technologies (CGT) Kinetics 4000 series cold spray system. The process gas was N_2, with a stagnation temperature of 600°C and a pressure of 3.0 MPa. The cold spray nozzle was held using an ABB IRB 2600 robot arm and moved in a raster pattern with passes spaced 1.2 mm apart to form 10 mm-thick deposits onto 1.6 mm thick 316 stainless steel. The robot traverse speed was 0.05 m/s.

Fig. 1 shows TEM micrographs of representative microstructural features observed towards the centre of a deposit (samples were electropolished and subsequently ion milled using a Gatan 691 Precision Ion Polishing System, Pleasonton USA). Due to the mechanics of particle deformation, the microstructure of cold-sprayed titanium is highly varied (Fig. 1a) with considerable grain refinement and formation of roughly equiaxed sub-grains. Fig. 1b shows one such region, with approximately randomly orientated sub-grains of the order of 0.1 - 0.2 µm in size. Regions with sub-grains below 100 nm have been observed in cold sprayed titanium [2]. There are also long bands and dark areas containing high numbers of dislocations (Fig. 1a bottom). Fig. 1c shows a dense dislocation tangle. Fig. 1d is a higher magnification image of an interface between particles, which runs diagonally from bottom-left to top-right. Amorphous layers are observed on either side of the interface. These layers are thought to be due to the high strain rates and rapid cooling in interfacial shear [3]. Although in most places along particle boundaries there was intimate contact and the boundary was often difficult to find, occasionally voids were observed, indicating poorer local bonding. Single particle studies have shown that interfacial voids are more

likely to be present at the base of the particle (the so-called south pole) compared to peripheral regions with more adiabatic shearing [4].
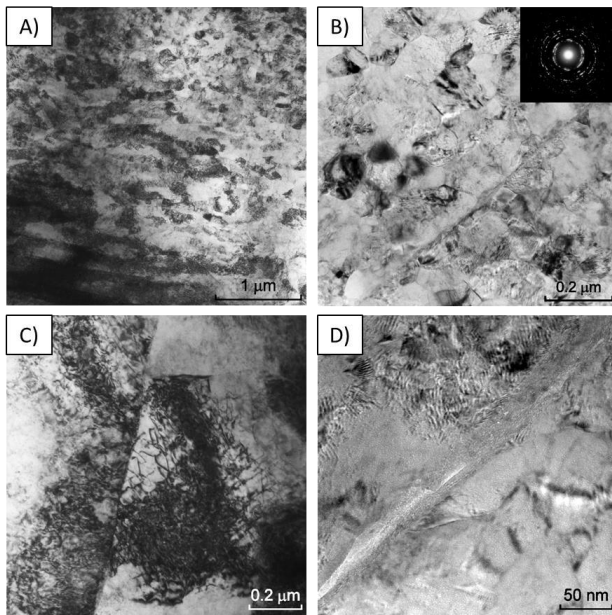

Figure 1. Bright field TEM micrographs of Grade 2 titanium in the as-cold sprayed condition. a) Low magnification image showing variability in microstructure, including b) sub-micron grains, c) dislocation tangles, and d) amorphisation at particle interfaces, as highlighted in the higher magnification images.

Due to the heavy dislocation loading, and incomplete metallurgical bonding at particle boundaries, cold spray deposits are typically brittle in the as-sprayed condition. There is generally little sign of plastic deformation upon failure, and fracture mainly occurs along particle boundaries. To achieve good mechanical properties from cold-sprayed titanium intended for structural applications, a post-spray thermal treatment is required, such as a high temperature anneal under inert atmosphere or vacuum, or thermomechanical processing via techniques such as hot rolling, extrusion, and forging.

1.2. *Hot isostatic pressing of cold sprayed titanium*

Mechanical properties following thermo-mechanical processing were investigated by manufacturing a cylindrical titanium billet using cold spray and then densifying by hot isostatic pressing (HIP'ing). The method invented to manufacture round billet by cold spray [5] allows uniform layers to be deposited axially at high rate due to the fast relative speed between nozzle and substrate. The nozzle can be tilted at the edges of the deposit to maintain a constant diameter [6]. An aluminium disc substrate was mounted on a lathe and rotated at 500 rpm. A CGT Kinetics 4000 cold spray system was held by an ABB IRB2600 robot arm, with the nozzle retracted each layer to maintain a constant standoff of 30 mm. The robot moved laterally across the diameter

of the disc, passing 1.0 mm either side of the rotational center (Fig. 2a), with a traverse speed inversely proportional to the radial distance from the axis of rotation and a minimum speed of 2 mm/s at the edges. The N_2 process gas and was set to 800 °C and 3.5 MPa in the stagnation zone. 2.5 kg/h of Grade 2 gas-atomised powder (Plasma Giken PG-PMP-1041, Saitama, Japan) was deposited, with the following key particle size characteristics; d10 = 14.5 µm, d50 = 29.5 µm, d90 = 47.4 µm. Optical microscopy (Fig. 2b) showed that the deposit had a uniform porosity distribution throughout.
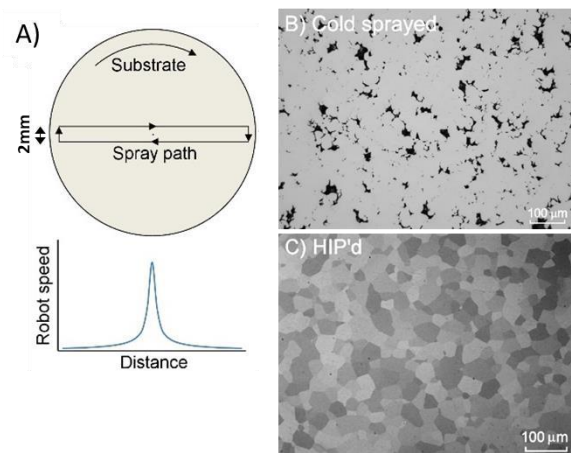
Figure 2. a) Schematic of billet production method [5] b) As-sprayed Grade 2 titanium with 5.6% porosity, c) Sample following canning and HIP'ing – under polarised light. Fully recrystallised grains are observed.

Following cold spray, the deposit was cut from the substrate, machined into a disk measuring 88 mm diameter and 20 mm thick, and then encapsulated in a steel can using standard fabrication techniques. It was then HIP'ed at 920°C at 100 MPa for 2 hours. The density of the billet following cold spray was measured using the Archimedes method and found to be 4.255 g/cm^3 or 94.4% of the theoretical value for Grade 2 Ti. After HIP'ing, the density was remeasured and found to be 100% of theoretical. Fig. 2c shows that a fully recrystallized microstructure was achieved and no porosity was observed. Oxygen and nitrogen concentration were measured at various locations within the disc using a Leco TCH600. Oxygen increased slightly from 0.15 wt.% in the powder to 0.18 ± 0.01 wt.% in the HIP'ed sample, while nitrogen increased from <0.01 to 0.02 wt.%, both well within the ASTM Grade 2 specification. Cylindrical bars were wire cut in the plane of the disc at different locations (Fig. 3a) and machined to produce tensile test samples with 4 mm gage diameter in accordance with ASTM E8M. The results showed a consistent ultimate tensile strength of 510 MPa, elongation of >30%, and maximum variation in elongation to failure of 7% (Fig. 3b).

Figure 3. a) Location of tensile specimens cut from HIP'ed Grade 2 titanium billet at different radial locations, b) stress-strain c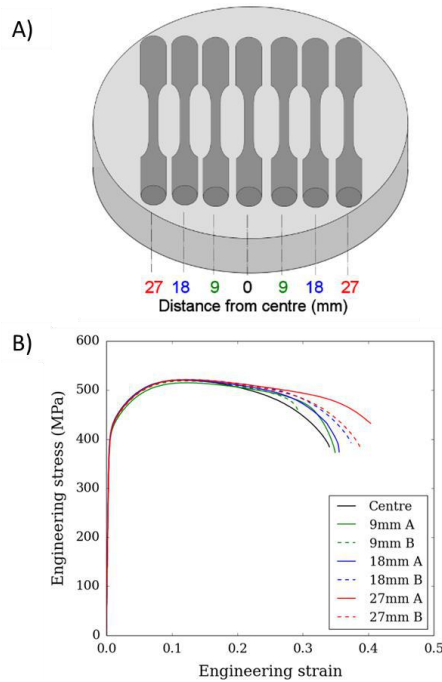urves showing similar tensile behaviour up to the ultimate tensile strength of 510 MPa. Elongation at failure was >30% and varied by 7% depending on location.

1.3. *Ti-TiC metal matrix composites*

With cold spray, it is possible to deposit unique combinations of powders including metal matrix composites (MMC's) comprised of metal-metal and metal-ceramic mixtures. In the latter, a continuous metal matrix phase can be reinforced with hard but brittle ceramic particles that form the dispersed phase. The ceramic particles do not deform during spraying due to their brittleness. Instead, they either adhere to the metal matrix through further matrix deformation or become embedded by subsequent incoming material [7]. The ceramic particles can provide a hammering effect, leading to densification and further cold working of the deposit, and repeated impingement of hard ceramic particles against the surface may also result in a surface activation effect by increasing substrate roughness and interrupting the oxide layer of the metal matrix, thus exposing clean metallic surfaces for enhanced metallic bonding [8]. Following heat treatment, the matrix phase can be recrystallised to produce the final, dispersion strengthened material.

A powder blend was made by mixing 90 wt.% Grade 2 titanium with 10 wt.% titanium carbide (Ti-10TiC). Spherical Grade 2 powder (AP&C, Boisbriand, Canada) was used with a particle size distribution of d10 = 19 µm, d50 = 28 µm, d90 = 38 µm. The TiC particles

(MSSA, Queensland, Australia) had an irregular morphology and a size distribution of d10 = 16 µm, d50 = 30 µm, and d90 = 43 µm. Rectangular blocks of Ti-10TiC composite material measuring 100 x 50 x 10 mm were deposited using an Impact Innovations (GmbH) 5-11 cold spray system. In all cases a water cooled OUT1 tungsten carbide nozzle was used with an expansion ratio of 6.2. The N_2 process gas was held at a stagnation pressure of 5.0 MPa. Two temperatures were investigated; 700 and 900°C. Powder feeder settings were selected to provide a feed rate of ~1.0 kg/h. Samples were deposited on aluminium plates and the nozzle was maintained at a constant standoff distance of 30 mm as the build progressed. A continuous tool path (Fig. 4a) was generated from an STL file using CSIRO's Continuous3D software [9]. The continuous path was made by executing two layers at a time, using the second layer to find return paths back to the start of each section, as described in [10]. A raster infill pattern was used which was rotated by 90° every second layer to produce a crosshatch pattern – a common technique in 3D printing to minimise anisotropic effects from unidirectional infill patterns. A nozzle inclination of 20° was used for contour passes to build more vertical edges [6]. The robot program was executed with one robot arm (ABB IRB4600) holding the cold spray gun while a second robot arm (ABB IRB2600) held the aluminium build plate. Build parameters for the various samples are summarised in Table 1.
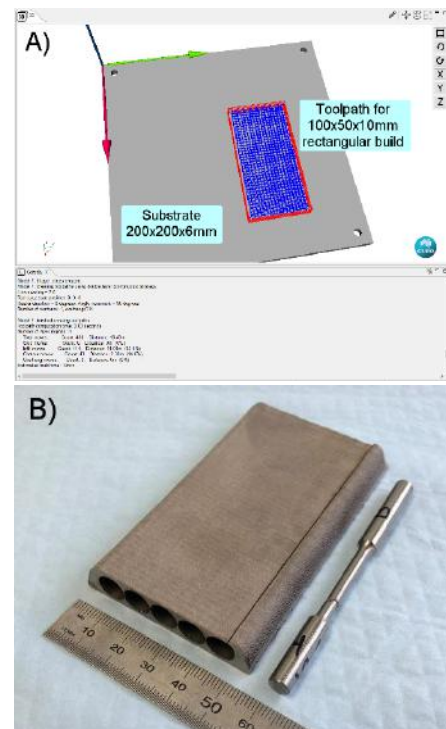

Figure 4. a) Toolpath generated via CSIRO's Continuous3D software [9]. b) Photograph of deposit following heat treatment and wire cutting.

Table 1. Build parameters and tensile properties for cold sprayed Ti-10TiC metal matrix composites after heat treatment.

Sample	1	2	3	4
Layer thickness (mm)	2.6	1.3	2.6	1.3
Spacing between raster lines (mm)	1.0	2.0	1.0	2.0
Gas temperature (°C)	700	700	900	900
Porosity (%)	6.43	6.01	4.07	3.03
Young's modulus (GPa)	106 ± 1.4	111 ± 1.3	115 ± 0.65	121 ± 2.6
Yield Strength (MPa)	420 ± 4.7	409 ± 3.1	513 ± 1.4	553 ± 17
Ultimate tensile strength (MPa)	481 ± 6.4	442 ± 36.5	575 ± 2.2	597 ± 8.6
Elongation to failure (%)	6.1 ± 1.1	3.4 ± 3.3	7.3 ± 0.23	11.0 ± 2.04

The cold sprayed material was removed from the build plate and post heat treated at 1100° C for 2 hours in a vacuum furnace (TAV-704, TAV Vacuum Furnaces, Bergamo, Italy) at a pressure of 5 mPa and furnace cooled. Following heat treatment, 5 cylindrical bars were produced in an identical manner to section 1.2 (Fig. 4b). Unlike HIP'ing, full densification was not achieved through heat treatment alone. Reducing the layer thickness improved deposit density, as compaction (or tamping) of deposited material is more effective with thinner layers. Density was also improved by raising the N_2 gas temperature from 700°C to 900°C, which produces greater particle acceleration and thermal softening of the material. This also translated to an improvement in strength and strain to failure, reaching almost 600 MPa and 11% respectively at the optimum settings. Cross-sections of the heat-treated samples (Fig 5a and b) show the carbide particles are well integrated and uniformly dispersed in the titanium matrix. X-ray powder diffraction indicated that some reaction may have occurred during heat treatment, forming a sub-stoichiometric phase (likely $TiC_{0.55}$) with smaller lattice parameters (Fig. 5c).

In summary, Grade 2 titanium particles are subject to intense plastic deformation during cold spray, yet the deposits typically retain porosity due to incomplete particle flattening and may contain unbonded interfaces. Heat treatment reduces porosity and improves

mechanical properties. By applying a thermomechanical process such as HIP'ing, full densification and excellent mechanical properties may be achieved. Second phase particles such as TiC can also be added to increase strength. Further investigation of powder combinations and thermal/thermomechanical treatments is warranted to fully realise the potential of cold spray for additive manufacture of structural titanium components.
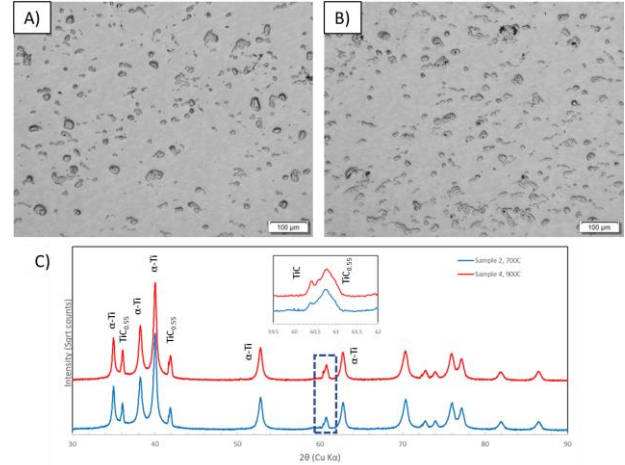

Figure 5. Optical micrographs of, a) sample 2 produced at a process gas temperature of 700C, b) sample 4 produced at 900C. c) X-ray powder diffraction data showing the presence of fully and sub-stoichiometric titanium carbide phases in both samples (peak splitting highlighted inset). Total carbide content was measured to be 7.6 and 9.6 wt.% for samples 2 and 4 respectively by quantitative Rietveld analysis.

2. TiWi - Converting waste powder forms to wire

Titanium wire is an important feedstock for large format wire-based AM and in the production of powder for powder-based AM. However, the cost of high-quality titanium wire produced by conventional mill processes is a significant barrier to broader adoption of wire-AM by mainstream industry. Meanwhile, thousands of tonnes of titanium swarf are generated each year by subtractive manufacturing processes. While this can be recycled via re-melting, swarf and other out-of-specification particulates represent a significant opportunity for repurposing via powder metallurgy methods.

The CSIRO's patented "TiWi" process [11] is designed to continuously convert low-cost titanium particulates, such as conditioned swarf, into high-value titanium wire for use in wire-based AM. TiWi is based on a modified version of the Conform extrusion process (Fig. 6). Wire diameters between 5 and 12 mm have been successfully demonstrated and a Science and Industry Endowment Fund (SIEF) project is currently underway to produce 3 mm diameter wire via a high torque extruder system, extending the technology readiness level to 6 (prototype verified) with batch sizes of up to 50 kg.
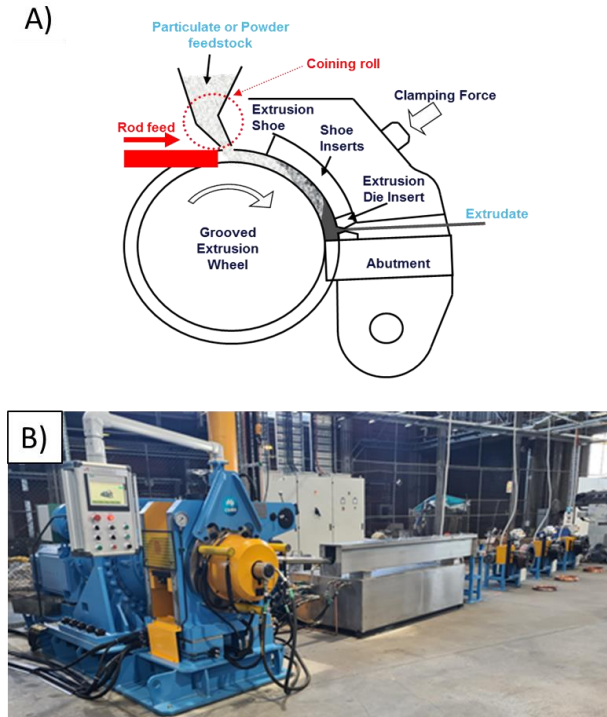
Figure 6. a) TiWi schematic showing both free-flowing particulate and pre-compacted particulate (rod) feeding methods b) Photograph of the TiWi line at CSIRO Clayton.

Table 2. Chemical analysis results (combined ICP-OES and inert gas fusion) from samples taken at 5 locations along the length of a 3.2 mm diameter wire produced by the TiWi process. Distances measured from the leading edge of the wire.

Location	0.2 m	3.2 m	6.4 m	9.6 m	12.6 m
Al (wt.%)	6.08	5.93	5.82	5.99	5.92
V (wt.%)	4.05	3.96	4.02	4.03	4.02
H (wt.%)	0.005	0.006	0.006	0.005	0.005
C (wt.%)	0.03	0.02	0.01	0.02	0.02
N (wt.%)	0.030	0.038	0.038	0.030	0.034
O (wt.%)	0.19	0.19	0.17	0.21	0.19
Cr (wt.%)	0.04	0.02	0.02	0.02	0.02
Fe (wt.%)	0.20	0.20	0.20	0.20	0.20
Co (wt.%)	<0.01	<0.01	<0.01	<0.01	<0.01
Ni (wt.%)	0.02	0.01	0.01	0.02	0.02
Mo (wt.%)	<0.01	<0.01	<0.01	<0.01	<0.01
Ti (wt.%)	Bal.	Bal.	Bal.	Bal.	Bal.

Wire lengths of up to 50 m of Grade 5 titanium have been produced from out-of-specification Grade 23 powder. Tensile properties of representative sections of the as-extruded wire include yield strengths of 1076 MPa and elongations of 9.3 %. Characterisation studies have been performed at various locations along the wires, to evaluate changes in chemistry and microstructure as process parameters tend towards steady-state operating conditions. Table 2 presents chemical analysis results for points along a 13 m length of 3.2 mm diameter wire, confirming that impurity levels are maintained within the specification for Grade 5. Fig. 7 shows a compilation of SEM images from samples taken at 0.2 m and 6.4 m along the extruded wire, confirming very low levels of porosity. At 0.2 m the microstructure is martensitic and there is some evidence of surface contamination (Co, Cr and W) from the tooling materials. At 6.4 m along the wire, surface contamination from the tooling material reduces and the microstructure becomes lamella. High resolution SEM-EDS analysis shows the surface oxide layer remains less than 1.5 µm in thickness.

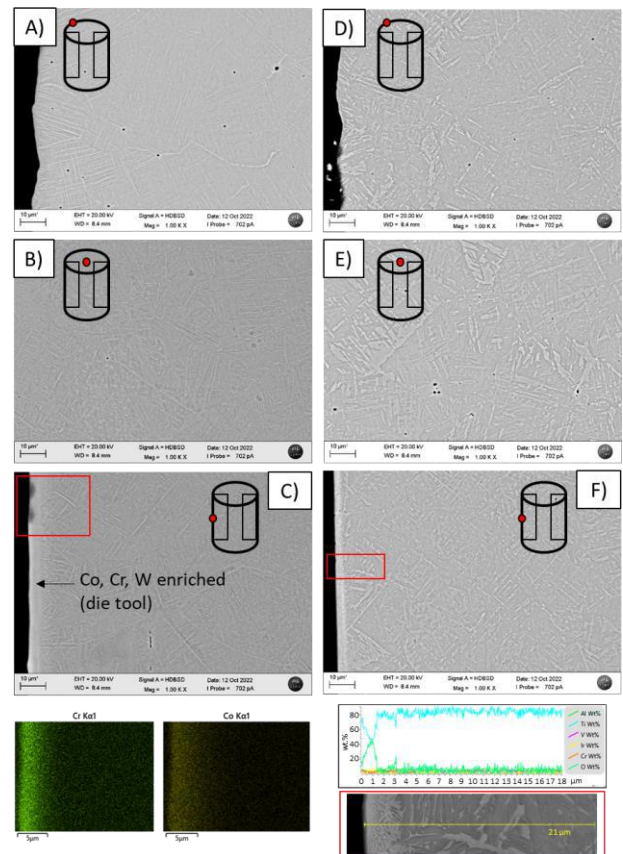Figure 7. SEM micrographs from 0.2 m sample: a) left transverse edge, b) transverse centre, and c) longitudinal left edge, with SEM-EDS map showing surface enrichment of Co and Cr from the die tool. Micrographs from 6.4 m sample: d) transverse edge, e) transverse centre, and f) longitudinal right edge, with high resolution SEM-EDS line scan showing surface oxygen enrichment confined to a depth of 1.5 µm.

Computational optimisation studies are currently being performed with respect to the die design. Preliminary results of time-resolved finite element analysis of the initiation of extrusion are presented in Fig 8. These results indicate that the leading edge of the powder compact can become constrained as it flows along the abutment into the die cavity, potentially leading to blockages in the lower holes of a multi-hole die arrangement. In addition to material flow, these simulations are being used to model thermal history of the wire and tooling during process start-up and subsequent operation, to understand and predict the properties of the extruded wire and wear mechanisms in the tooling.
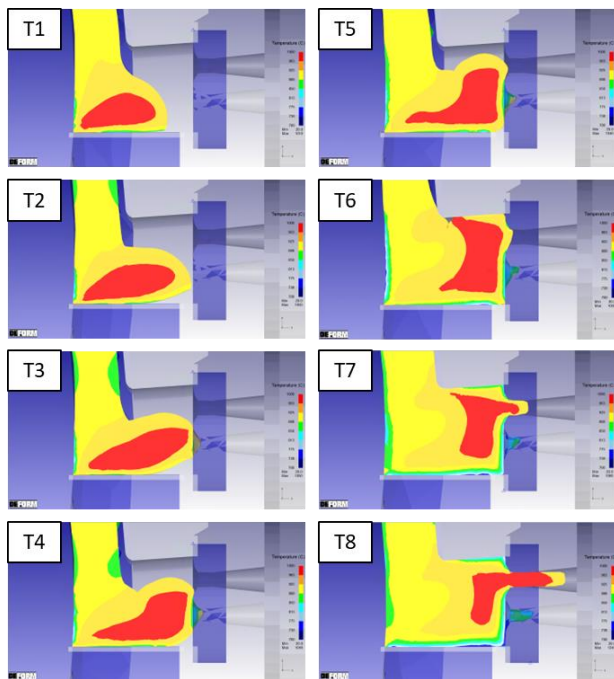

Figure 8. Results of time-resolved finite element analysis of the initiation of extrusion in the TiWi process using a 3-hole die arrangement, showing material preferentially exiting the top-most hole (time increments are denoted T1 to 8).

3. Acknowledgements

4. References

[1] M.Z. Jahedi, S.H. Zahiri, S. Gulizia, B. Tiganis, C. Tang, D. Fraser, Direct Manufacturing of Titanium Parts by Cold Spray, *Materials Science Forum.* 618–619 (2009) 505–508.

[2] P.C. King, M. Jahedi, Transmission Electron Microscopy of Cold Sprayed Titanium, in: ASM International, 2010: pp. 4–9.

[3] Y. Xiong, K. Kang, G. Bae, S. Yoon, C. Lee, Dynamic amorphization and recrystallization of metals in kinetic spray process, *Applied Physics Letters.* 92 (2008) 194101.

[4] P.C. King, C. Busch, T. Kittel-Sherri, M. Jahedi, S. Gulizia, Interface melding in cold spray titanium particle impact, *Surface and Coatings Technology.* 239 (2014) 191–199.

[5] P.C. King, S. Gulizia, A.J. Urban, J.E. Barnes, Process for producing a preform using cold spray, WO2015157816A1, 2015.

[6] J. Pattison, S. Celotto, R. Morgan, M. Bray, W. O'Neill., Cold gas dynamic manufacturing: A non-thermal approach to freeform fabrication, *International Journal of Machine Tools and Manufacture.* 47 (2007) 627–634.

[7] A. Sova, M. Doubenskaia, E. Trofimov, M. Samodurova, V. Ulianitsky, I. Smurov, Cold Spray of Metal Powder Mixtures: Achievements, Issues and Perspectives, *Trans Indian Inst Met.* 74 (2021) 559–570.

[8] S.V. Klinkov, V.F. Kosarev, Cold Spraying Activation Using an Abrasive Admixture, *J Therm Spray Tech.* 21 (2012) 1046–1053.

[9] F.N. Lomo, A. Vargas-Uscategui, P.C. King, M.J. Patel, I.S. Cole, Microstructure and mechanical properties of heat-treated cold spray additively manufactured titanium metal matrix composites, *Journal of Manufacturing Processes.* Accepted (2023).

[10] P. King, A. Vargas Uscategui, A Method of Determining a Tool Path for Controlling a Printing Tool, WO2021016666, 2021.

[11] R.S. Wilson, M. Yousuff, N.A. Stone, D.J.B. Ritchie, G.M.D. Cantin, M.A. Gibson, I.C. Thomas, Extrusion of high temperature formable non-ferrous metals, US9468960B2, 2016.

TITANIUM ALLOYS WROUGHT PROCESSING STATUS AND PROGRESS

Michael Leder, Anatoly Volkov, Vladimir Kropotov, Eelizaveta Plaksina

PSC VSMPO-AVISMA Corporation, Parkovaya st. 1, Verkhnaya Salda 624760, Russia

Since the last conference, new challenges of deformation technologies have been added to the existing one: additive technologies and a permanent request to reduce BTF. The world was facing the global challenges of the COVID19 pandemic in 2020-2021 and the threat of a global economic recession in 2022. These events significantly changed the market, supply chains, and financial flows. The decrease in air traffic (up to 90% at the peak) caused by the closure of borders led to a decrease in aircraft production rate, respectively, a decrease in the speed of their production, which cooled the market for the all supply chains, including titanium materials. The two traditional requests of reducing material costs and increasing supply chain reliability will intensify dramatically under the threat and consequences of an economic recession. This makes us take a fresh look at the optimization of deformation processes using a reasonable choice and refinement of technological ranges, optimization of tools and workpieces, approaches to the development of the process.

1. Introduction

All the main practical directions and methods of plastic deformation were developed in the 19th century in application for structural steels and in many respects were successfully adapted for titanium alloys taking into account their features: low thermal conductivity, high viscosity, tendency to sticking, gas saturation, hydrogen embrittlement, etc. At the moment, most of the methods: free forging, pressing, sorting and sheet rolling, drawing, etc., are very detailed for particular cases of geometries, mechanical properties and alloys classes. Manufacturers need only to optimize the processes of deformation using a reasonable choice and refinement of technological ranges, optimization of tools and workpieces, approaches to the development of the process. Despite partial repetitions and re-discoveries of already well-known progress, it did not stop, but simply moved to other levels and scales, and without becoming less interesting and succinct, although it may be, giving less ambitious results.

2. Results and discussion

2.1. General situation

Despite the potential threats from alternative technologies: powder technologies and additive technologies, according to [1], the forging business is growing steadily enough: 60% of surveyed companies stated growth in 2018 by + 5 ÷ 25%, and also in the forecast of growth in 2019 year at about the same pace. For 5 years from 2014, relative stagnation of growth was observed only on the results of 2 years: 2014 and 2017. According to the prevalence of production, titanium alloys, of course, cannot compete with carbon , alloyed and stainless steel, which produce > 50% of forging companies.
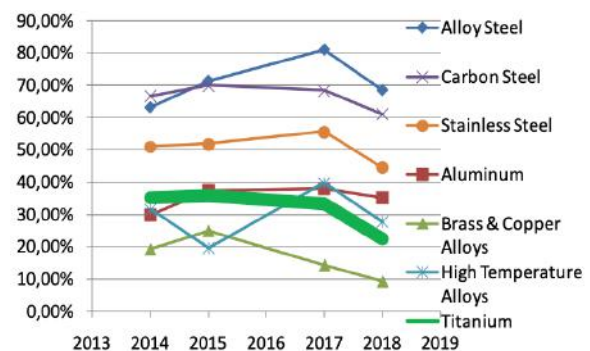
Figure 1. Material, forging companies work with

But titanium alloys are comparable in prevalence with Al and hi temperature alloys (Fig. 1), possibly due to use in the same aerospace region. In 2018, almost 20% decrease in the number of forging companies producing titanium and hi temperature alloys, even with the normalization of the results (Fig. 1 c). It is difficult to reconcile with the growing market for aerospace and it is possible that this result is due to the change of the spectrum of companies of choice, or a decrease of number of players due to market globalization wrought titanium alloys .

Figure 2. Actual problems of forging companies.

The results of the analysis of the spectrum of problems experienced by forging companies are also very positive (Fig. 2). On background stable topical parameters energy cost , foreign competition , and less sensitive

availability of capital , raw material lead-time, raw material quality is observed growth Relevance labour shortage, higher labour costs, and in last 3 years drastically increase of raw materials costs. But all these problems fade into the background when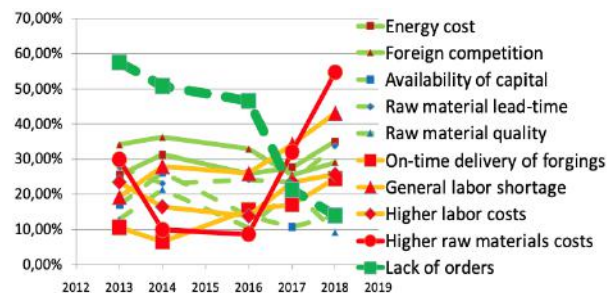 there are orders in the market: only 14% of companies experienced a shortage of orders in 2018, despite the fact that in 2013 there were about 60%.

2.2. *Market inquiries*

Of the 3 main market inquiries before wrought titanium companies: increase operational properties of materials, reduce lead time, cost reduction , bright cost was dominated by the dominant gain reduction . Such same old, and friend, how all wrought processing of titanium alloys. To meet this market demand, manufacturers work in the following directions: increase by-to-fly ratio, reducing the cost of batch materials, increasing the involvement of waste, reducing the cost of deformation and heat treatment, increasing the processability of the material and the efficiency of processing methods, reducing the working cost further.

Taking into account the excellent work on the optimization of production costs, it is necessary to understand that the manufacturing technology of titanium semi-finished products is currently highly optimized. Further cost reduction, along with the inevitable decrease in quality, at a certain level will lead to a sharp increase in the risk of inconsistencies or negative side changes in the material\part properties (Fig. 2). Moreover, these discrepancies will no longer be typical, the quality management system is set up to identify and eliminate them. The unusualness of these inconsistencies can be missed by the QMS and give poorly predictable consequences of the use of such material. The critical level of risk increase is difficult to predict, as this is an unknown factor. Categorical cost reduction works as an accumulation of "explosive substances" that can" detonate" when the critical level is exceeded.

There are alternatives to reduce the cost by increasing the operational properties of the material which could not only reduce the cost, but also increase the operational characteristics of the structure.

With increasing the specific strength of the cross section of the part can be reduced, which not only leads to a decrease in cost by reducing the weight of the workpiece, but also reduces the weight of the structure - one of the most important performance characteristics.

At the moment, the level of the basic strength of titanium alloys can be considered the level provided by the Ti-6Al-4V alloy , which in sections over 100 mm can provide UTS > 1050 MPa, and in sections <30 mm up to UTS = 1200 MPa. The VST 55531 alloy is able to provide up to 1600 MPa in sections up to 5" UTS , and up to 1750 MPa in limited processing of simple sections with certain treatments [2]. This will ensure up to 1.5 times the reduction of the cross-sectional area of the part (simplified construction).

Of course, the VST 55531 alloy contains significantly more relatively expensive alloying materials, which increases its cost. In most cases, classical high- strength alloys can be replaced with an economically- doped VST 2 alloy , which includes a large number of waste Ti-6Al-4V, VST 55531 , a sponge of low purity and cheaper Fe master alloys [3].
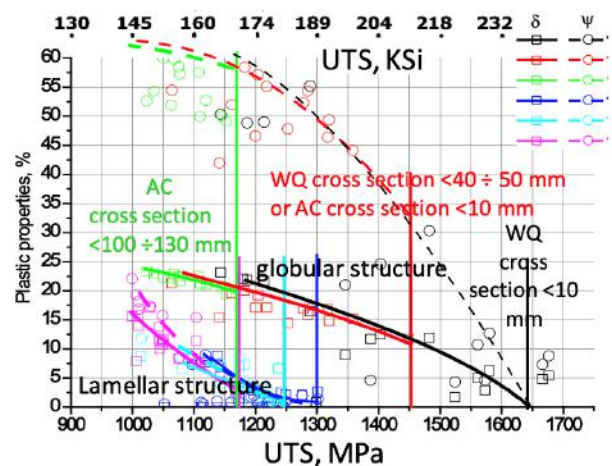
Figure 3. Mechanical properties VST2 alloy.

Alloy VST 2 is able to provide up to UTS < 1650 MPa when hardening sections less than 10 mm, UTS < 1450 MPa when hardening sections less than 50 mm and UTS < 1170 MPa when annealing sections less than 130 mm. It can also provide a maximum reduction in cross-sectional area (mass) up to 1.35 times. (Fig. 3)

Increased material fracture toughness increases damage tolerance and can also provide a reduction in the cross-section of the part. So on the alloy VST 55531 can be increased K1c material by about 17% relative to the level of alloy Ti-6Al-4V with a lamellar structure (Fig. 3)

Conditionally sharing wrought processing on Areas: Equipment development, Stock development, Process development, Material behaviour can be characterize.

2.3. *Equipment development.*

Despite the substantial risks posed by relatively new additive technologies, confidence in the demand for traditional technology remains high. A vivid confirmation of this is the purchase of powerful new press equipment. In Q2 2015, the Nanshan press was commissioned. Forge Company production Siempelkamp Pressen (Germany) [4]. Since the conclusion of the contract, the project has been extended for 3 years. During its creation, Siempelkamp broke its own casting record of 301 tons, making the casting lower press A beam weighing 320 tons. The press has the following parameters:

- Force: 50 thousand . Tonn (MH 500)
- Working stroke speed: 0.05-50 mm/s
- Stroke : 2000 mm
- Die clamping area (working table): 4000 x 7000 mm
- Number of master cylinders: 8, effort 61.3 MN
- Hydraulic system : 60 pumps, total power 24 MW, volume of hydraulic oil 180 m^3, working pressure 420 bar (428 atm)
- Open space between columns: 5 x 3 m
- Modes of working stroke: compensation of eccentric loads; with control by strain rate; ultra-low speed
- Dimensions: height 30 m
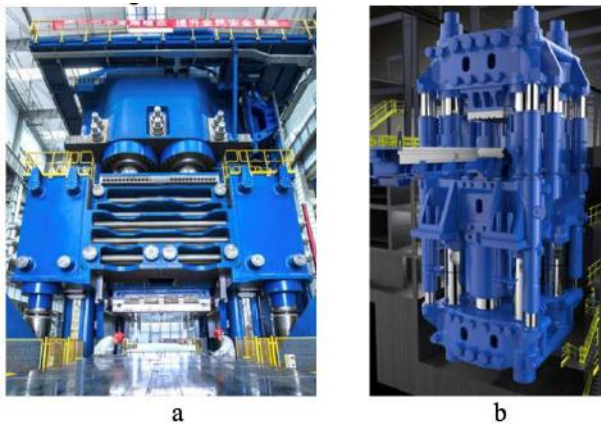- Weight: 7.5 thousand tons.

Figure 4. Presses a) Nanshan Forge Company (China) b) Weber Metals and OTTO FUCHS KG (US)

In October 2018, an enchanting presentation of the Weber press took place. Metals and OTTO FUCHS KG (US) produced by SMS Meer (Germany) [5]. The project took just over 2.5 years and cost $180 million. This press is considered the most expensive purchased for private investment. Technical options press:

- Force: 540 MN
- Stroke: 2000 mm (79 In)
- Die clamping area: 6000 x 3000 mm (236 x 118 in)

Figure 5. Ring rolling mill RAW 400/200-3500/800

On VSMPO In the 2nd quarter of 2017, a new complex from the ring rolling mill RAW 400 / 200-3500 / 800 and the ring of the blank press with a force of 8,000 tons by the manufacturer SMS Meer (Germany were put into operation (Fig.5). The general increase in the processing efficiency makes it necessary to use complex devices and equipment ensuring maximum form change in a single pass of deformation [8]. The developed tooling consists of 3 embossed rollers with stepped forming protrusions, the combination of the translational and rotational movements of which allows the wall of the pipe billet to be reduced several times in a single pass (fig. 6).
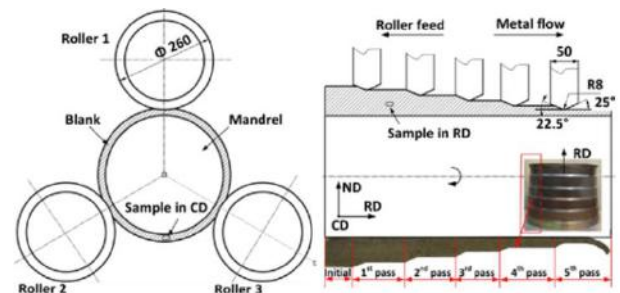

Figure 6. Three embossed rollers with stepped forming protrusions.

The control surface of the workpiece at a line of production was always relevant, especially with a small semi readout during machining. To control the quality of the bar stock, a shadow scheme was known in which, according to the size of the source shadow light could control the diameter of the rod. The company Kocks introduced to this technology the measurement of the surface profile using a laser [9]. Laser scanning of the bar surface with a frequency of up to 2000 profiles per second from 4 sides allows you to form a complete surface profile with an accuracy of ± 0.025 mm. Of course, at the moment the surface profile obtained with inline scanning with speeds up to 10 m/s cannot be used to meet the requirements, but at scanning speeds of about 0.5 m/s, the surface profile turns out to be detailed and quite suitable for assessing requirements.
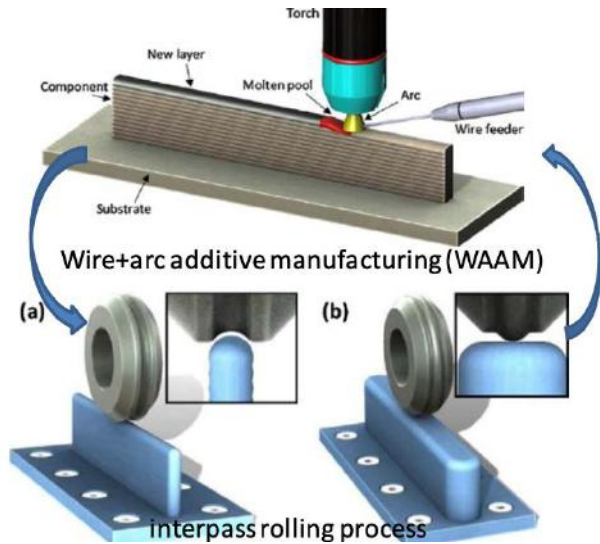
Figure 7. Hybrid technologies

Hybrid technologies based on additive ones provide quite interesting methods of deformation. As is known, all additive technologies conduct metal through melting, in the case of DMD - multiple, therefore the creation of deformed structures is impossible. However, a method has been proposed for the local deformation by the synthesized surfacing of a wire wall by rolling with a roller, which has a concave profile for relatively thin walls and a convex profile for thick walls [10] (Fig.7). The radius of the bulge may vary. After synthesis, the roller is rolled along the entire surface of the rib. With sufficiently small effort, it is possible to deform the synthesized layer with a degree of deformation sufficient to reduce the b-grain from several millimeters to tens of microns. With increasing degree Deformation by increasing the pressure and number of passes, the grain size used after synthesis is reduced. It should be noted that this technology is relatively easy to scale to thick sections, but the problems of deformation of sections / wall thickness of a few millimeters are obvious.

2.4. Stock development.

Solving the problem of tightening the dimensional tolerances while reducing the cross-section of parts like profile, as well as reducing the cross-section of these parts suggested the use of stage processing [11]. At the first stage, a billet is obtained by high-performance methods, but not allowing to obtain very thin walls with the necessary tolerance. In the second stage, the walls are thinned by rolling to obtain very thin walls with tight tolerances, an increase in BTF, a more uniform deformation over the cross section. In the case of cold rolling it is also possible to use strain hardening.

One of the most relevant areas for the development of a blank is the use of a "hybrid" blank, i.e. obtained by methods of traditional extraction technology [12] (fig.8). Most common embodiment 3: Synthesis of the preform using conventional powder metallurgical methods of synthesis of the entire workpiece AM, hybrid preform. A hybrid billet consists of a part (more often, a slab) of the traditional technology obtained with the addition of elements to it by methods of additive technology. Additive technologies are understood in the broadest sense. Preparation: powder, wire. A source heating: electronic beam, laser , plasma, electric arc. direct metal depositions. Powder bed of direct metal depositions.
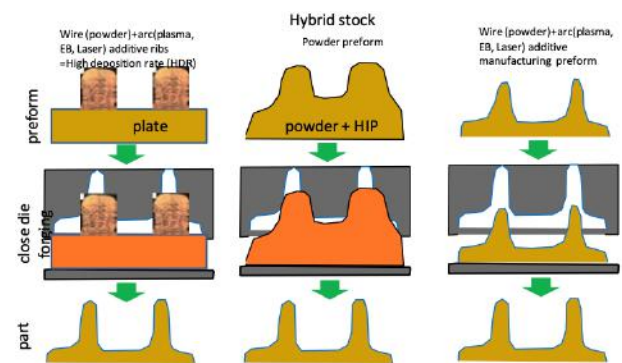

Figure 8. Hybrid stock

The preform is subjected Deformation (usually stamping) scheme billet made by conventional method. It is clear that by hybrid and powder methods it is difficult to obtain a billet of a complex shape, therefore these billets will have a maximum allowance relative to the final geometry. AM the stock will have a minimum allowance. Currently AM synthesis speed even in the case of High Deposition Rate (HDR) is several times lower than powder and traditional, which causes a longer cycle of preform creation using AM , proportionally increasing the cost of their synthesis.

Raw materials in the form of surfacing wire and powder are significantly more expensive than traditional billets, besides powder preforms must be subjected to HIP and follow further processing to remove the container. All of the above casts doubt on the effectiveness of the hybrid billet in terms of cost reduction.

From the point of view of the quality of the material, it is necessary to understand that all the synthesized elements will have a cast structure, respectively, will be subjected to deformation only at the final stage with very small degrees of deformation. This is especially important for layer-by-layer synthesis, in

which epitaxial growth of β- grains is observed up to a size of several millimeters in the direction of the deposition front [13]. Deformation at α + β areas not eliminates given structure . For a relatively equiaxed β- grains, it is necessary to carry out recrystallization annealing in the β- region after preliminary deformation with a degree of at least 30–40% in the α + β or β region. The need for this β- recrystallization annealing also imposes restrictions on the technology of working with a hybrid billet.

2.5. Process development

Deformation gamma intermetallic compounds is important stage in the development of their production, as the most promising high-temperature alloys. The duplex structure of the deformed gamma aluminides provides increased ductility, strength and fatigue strength with an acceptable reduction in heat resistance. The problem is a very high strain resistance, which makes non-isothermal deformation (especially thin sections) very difficult , and leads to the necessity of switching to low strain rates realized in isothermal conditions. The higher metal utilization ratio (CIM) of isothermal punching is balanced by the high costs of the tool and makes it profitable only for mass production. Deformed blades of gamma aluminide are planned to be used in the PW 1100 [15]
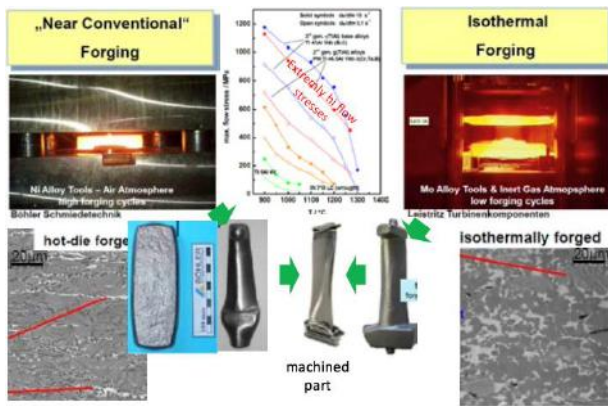

Figure 9. Deformation gamma intermetallic.

When stamping products of a large projection area, a condition of insufficient pressure of the existing presses occurs. AT by this case applied sectional stamping, with which happens phased registration separate areas. This technology has been used by many companies since the 70s and 80s. In this technology, there are a large number of challenges: defects in the form of clamps and flash, folds of buckling, neoformaniya, which are traditionally solved by trial and error, leading to significant costs during development. A group of authors approached the problem of forming very systemically: a

rheological model of the material and structure was constructed , the model was verified, a through iterative simulation of the process of forming was carried out with the identification and elimination of problems, which made it possible to obtain sectional stamping with work [16,17].
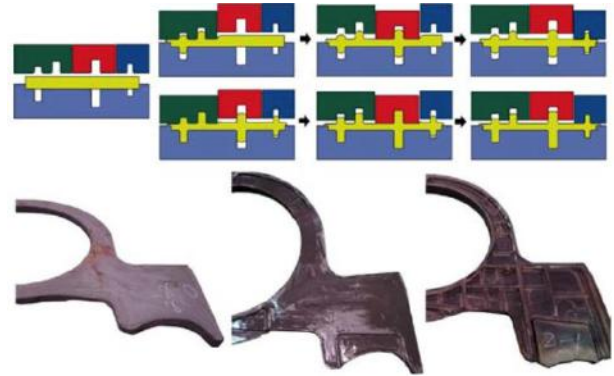

Figure10. Section die forging.

2.6. Modelling

Most intensely developing direction at alloys is a plastic deformation simulation. The most developed and widespread method of modeling is the finite element method. Finit Element Modeling (FEM). In recent years, they try to give modeling the status of end-to-end not only by transitions, but also by spheres, adding to modeling plastic deformation, modeling structure and texturing, with the ultimate goal of modeling mechanical properties.

The classical FEM plastic deformation modeling based on the rheological data of the alloy currently covers all technologies, allowing you to get the T , ε, fields on all transitions: forging, stamping, sheet and section rolling, ring rolling. Classical FEM modeling allows simulating the residual stresses during quenching with non-equilibrium conditions [18].

It also simulates the stress state of the tool to assess its working conditions and durability.

In the classical version of FEM , even under conditions of a complex combination of cooling and adiabatic heating, the accuracy of temperature modeling does not exceed 5°C in most cases [19]. The accuracy of modeling geometric dimensions does not exceed 7% [20]. More difficult is the accuracy of the prediction of the strain effort, since it is very dependent on the parameters of friction and the accuracy of the boundary conditions, but for most simple geometries it does not exceed 15%.

The main direction of the development of modeling is the modeling of microstructure parameters.

The most common parameters for α+β- alloys are the proportion of the primary α-phase, the size of the primary α-phase, and the degree of spheroidization.

With a sufficiently significant difference in particular, the modeling process as a whole is structured according to one scheme: conducting an experiment, building a model for the formation of structures, integrating the model for structure- forming into the FEM module, and solving boundary value problems.

In work [21] on the alloy Ti-6Al-2Zr-1Mo-1V an analytical model was used to change the proportion of the primary a-phase ($\gamma_{\alpha 1}$), the size of the primary a-phase ($b_{\alpha 1}$). The verification of the model of structure formation took place in experiment 2 of stage deformation in the range T=910-970°C with ε=50%, ὲ=0.011/s. The solution of the boundary-value problem 2 of staged sectional stamping in the package of the commercial package DEFORM made it possible to obtain divergence with experiment for $\gamma_{\alpha 1}$ - up to a maximum of 22.2% on average 9%, for $b_{\alpha 1}$ - to a maximum of 16.7% on average 8.8% (Fig.10).
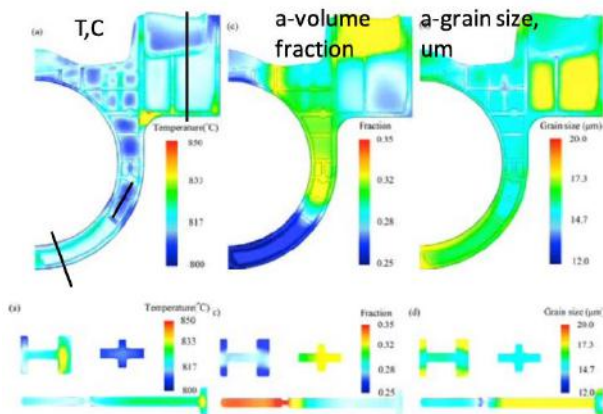

Figure 10. DEFORM model of Ti-6Al-2Zr-1Mo-1V forging

In work [22] on the Ti-6Al-4V alloy, the artificial - neural - network (ANN) model of structure formation was carried out on a series of experiments with variation in a wide range of T, ε, ὲ deformation, with simulated isothermal exposures. The solution of the boundary-value problem of isothermal punching made it possible to obtain a divergence with experiment for $\gamma_{\alpha 1}$ <10% , and for non- isothermal <30% in some cases, the differences up to 5 times. The divergence with experiment $b_{\alpha 1}$ was <20%.
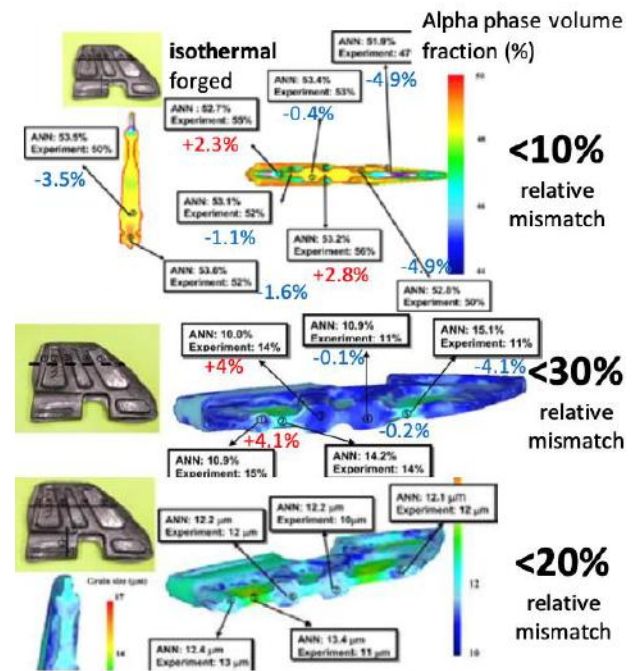

Figure 11.

Significantly smaller difference in level raskhozhde Nia with experimental results operation result [21] with substantially less wide array verification experiment result emphasizes the great strength and stability predictive analytical model microstructure . In this case, there always remains the question of monotony and continuity of the function of the magnitude of the error (discrepancies with experiment)- are large quantities possible?

In the direction of end-to-end modeling (deformation - struktkura - mech . From the estate), a very ambitious project was launched with the participation of a very representative circle of scientific organizations, consumers, manufacturers of titanium alloys: Rolls-Royce, Boeing ,General Electric Aviation, Pratt & Whitney, Computherm, Cornell University, Scientific Forming Technologies, Materials Resources LLC, PCC - Wyman - Gordon, ATI Forged Products, TIMET, Air Force Research Laboratory [25] . Filled in the form of additional plug-ins to the commercial program DEFORM scheduled model parameters duplex microstructure alloy Ti 6 Al 4 V ($\gamma_{\alpha 1}$, $b_{\alpha 1}$, $b_{\alpha 2}$) parameters plate structure (size β- grain D_β , $b_{\alpha 1}$, colony size primary α-phase ($d_{\alpha 1}$)) crystallographic texture of the primary and secondary α-phase , short-term mechanical properties. A colossal work on model verification is planned. The first results show tremendous complexity of this work: modeling of texture secondary α- phase koordinalno vary depending on the detail of the grid used. The announced

current deviation of model mechanical properties from experimental ± 5% is impressive at first glance. However, the scatter 10% UTS is approximately 100 MPa, which amounts to 28% of the total range of variation UTS = 1200-850 = 350 MPa for the alloy Ti-6Al-4V. The minimum acceptable accuracy of the simulation results for using them as reference can be considered ± 10 MPa , i.e. 5 times lower than the current level. This again indicates a large amount of work ahead.

In a simulated parameter may be not only the parameters of the microstructure, but also any material parameters podver gayuschiesya quantify, for example, ultrasonic (UT) material properties. In [23], the relationship between the parameters of the ultrasonic signal (its noise component) and the anisotropy of the β-grain of the Ti6246 alloy was studied experimentally . A model of the ultrasound effect was developed, which is integrated into the FEM module. As a result, developers of the deformation technology have the opportunity to model the ultrasonic properties of the material, which made it possible to optimize them, in cases where other parameters allow it.
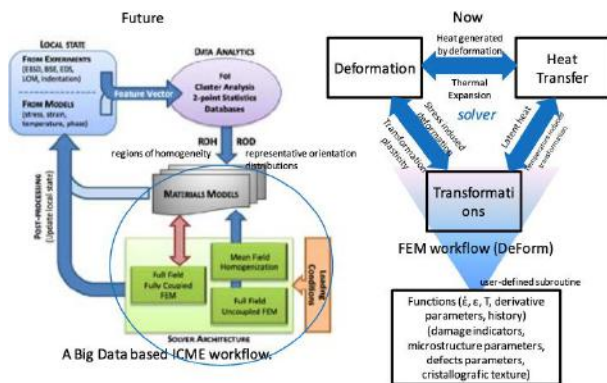

Figure 12. Routes of microstructural models relations.

At this stage, the microstructural change models work at the post processing stage in the form of private modules. This happens separately from the FEM solver, which takes into account only elasticity, rheology, heat transfer, and special cases of phase transitions (Stress indused deformation, Transformation plasticity). In reality, a change in microstructure, texture leads to a change in rheological properties. This should be taken into account in future deformation models in which the model strutkury material (material models) will work in the composition or closely solver [3]. Probably, this will make it possible to further clarify the results of modeling shaping and struktkury.

Despite the undeniable advantages that modeling gives about 40% of forging companies, even classical modeling does not use for very simple reasons: cost and staff qualifications. And their share has not decreased since 2014. This somewhat "cools off" the development of modeling.

2.7. *Material behavior*

Plastic deformation modeling requires knowledge of the material's response to an external effect. In this case, the classical approach to the description of the deformation behavior is various model approximations of the rheological compression curves. Additional processing of data by the methods proposed by Prasad , YVR allows to reveal the regions of temperature and strain rates in which instability\localization of deformation is possible, which is very important data for combating deformation cracks that are not obtained by other means. An additional analysis of the microstructure of the deformed samples makes it possible to identify areas of structural transformations and obtain a map of the deformation mechanisms [26, 27]. For example, for 6-4, to divide the area of globularization , creasing of plates and adiabatic shear bands, as well as to distinguish the area of grain- boundary cracking. For pseudo- beta alloys, separate the areas of dynamic recrystallization and recovery, and the areas of adiabatic shear bands (localization).

The areas of strain instability in the general case are quite strongly dependent on the degree of deformation, which must be taken into account and taken into account when using [28] . Although it is possible to trace the kinetics of changes in instability areas by the results of some data on the dependence of flow stress on the degree of deformation, simply by analyzing them at different degrees of deformation. More difficult with maps of deformation processes, for which the analysis of structures is necessary, i.e. additional experiment on the deformation to a given degree. This makes the processing map analysis relatively versatile.

Processing map @ deformation mechanisms map is very sensitive to changes in the original structure and chemical composition. Reducing oxygen within the alloy grade Ti-6–4 from 0.18 to 0.13 significantly and increasing the thickness of the plates of the primary a-phase by about 2 times, the maximum temperatures of the prior b-boundary cracking and adiabatic shear bands decrease from 900 to 800°C, and The limiting deformation rate ensuring the spheroidization of the α phase grows by an order of magnitude from 10^{-2} to 10^{-1}

[26, 29] . In this case, the question remains open about the accuracy of determining these areas.

One of the drawbacks of processing maps is the unknown accuracy of the calculation of the energy dissipation efficiency (nu) and the range of flow instability (k or e) [27]. Being within the same approximation, slightly different ways of calculating nu and k give them a very significant change. In practical terms, this complicates the process of choosing the optimal deformation mode.
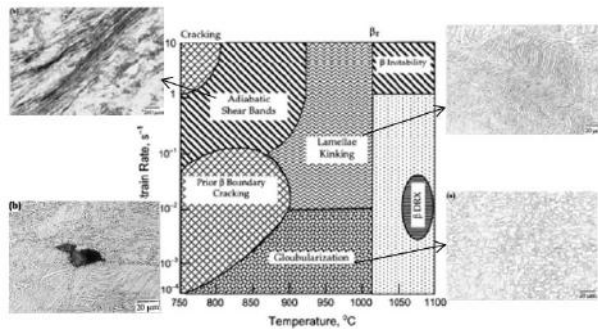

Figure 13.

Another limitation is that even deformation in an area free from localization and grain boundary cracking can lead to the formation of deformation defects, primarily on the surface. This speaks first of all about the existence of additional important factors, which do not take into account this approximation.

Despite the large amount of research and data on the deformation behavior (rheology) and the evolution of the microstructure during the deformation process, very little attention has been paid to the effect of stops / interruptions during deformation on the deformation behavior. In recent works [30], it was shown that at holding up to 10 min in the a + b region with large strains (> 0.4) does not lead to significant softening, and repeated loading does not lead to re-strengthening above the level before the interruption.

In the region of small deformations in tension, no significant changes in the flow stress after interruption [31, 32] are also observed , despite the fact that the stress relaxation significantly increased with increasing temperature.

3. Conclusions

The paper examines the main development trends of wrought processing of titanium alloys . Despite the high level of development and mastering of the main methods and directions in wrought processing , there

remain enough areas of development and optimization of which gives tangible practical results.

4. References

1. Titanium International, 3-9 2022, Flightglobal. 2014-2018 FORGING BUSINESS OUTLOOK.
2. Technical report, unpublished work.
3. Leder M.O., Tetyuhin V.V., Volkov A.V., et al.. AEROMAT 2017, Charleston, SC, April, 2017
4. www.nanshanforge.com; www.siempelkamp.com.
5. www.otto-fuchs.com/en/business-areas/aerospace-industry/asg-group-60k.html
6. www.vsmpo.ru
7. D.Lazorkin. High performance thechnology and equipment ..., ITA2018
8. Wang, X.X., et al., 2018. *J. Mater. Process Technol.* 261, 86–97.
9. Glyn Ellis, 4D eagle: the new gauge from Kocks for bar and wire rod quality, Titanium USA 2017.
10. McAndrew, A.R. et al., 2018. *Addit. Manuf.* 21, 340–349.
11. US 2017 / 0306467 A1 Oct.26, 2017
12. US 2015/0013144 A1 Jan. 15, 2015
13. Semiatin, S.L., Kobryn, P.A., et al., 2001. Metall. Mater. Trans A 32, 1801–1811.
14. US 2018 / 0347003 A1 Dec 06, 2018.
15. Smarsly, W., 2016. Status of Titanium Aluminide for Aero Engine Applications, Titanium Europe 2016, Paris, France.
16. Zhang, D.-W. et al, 2018. JAMT 99, 1427–1448.
17. Fan, X.G. et al, 2014 *J. Mater. Process Technol.* 214, 253–266.
18. de Oliveira, M.et al, 2002 *JMEP* 6., 11, 80-85.
19. Venkatesh, V., et al., 2009. JOM 61, 45–50.
20. Fan, X.G., Yang, H., Gao, P.F., 2014. *J. Mater. Process Technol.* 214, 253–266.
21. Fan, X.G., Yang, H., Gao, P.F., 2014. *J. Mater. Process Technol.* 214, 253–266.
22. Kim, J.H., et al., 2009. *Metals and Materials International* 15, 427–437.
23. Y. Ito, et al., 2015,TiUSA2015.
24. Salem, A.A., et al., 2014. *Integrating Materials and Manufacturing Innovation* 3.
25. M.G. Glavicic, et al, 2016, Proceedings of the 13th World Conference on Titanium, 1867-1873
26. Seshacharyulu, T., et al, 2002. *Mater. Sci. Eng: A* 325, 112–125.
27. Dikovits, M., et al, 2014. *Metall. Mater. Trans A* 45, 1586–1596
28. Nie, X., et. al. 2014. *Mat. Sci. Eng.:A*613,306–316
29. Tamirisakandala, S. et al, 2001,*JMEP* 10,125-130.
30. Fan, X.G., et al, J. Mater. Sci. 2011, 46: 6018-6028
31. Julien, R., et al., *Mater. Lett.* 2017.
32. Julien, R., et al., *Int. J. Mech Sci*. 2018.